



# Application of high-level Green–Naghdi theory to sill-controlled flows

Oscar Castro-Orgaz<sup>1</sup> · Pedro P. Gamero-Ojeda<sup>1</sup> · Francisco N. Cantero-Chinchilla<sup>1</sup> · Tomás Morales de Luna<sup>2</sup> · Hubert Chanson<sup>3</sup>

Received: 1 June 2023 / Accepted: 29 November 2023 / Published online: 4 January 2024  
© The Author(s), under exclusive licence to Springer Nature B.V. 2024

## Abstract

Sill-controlled flows involving the acceleration across a crest or control section with significant flow curvature are characterized by the Euler equations of an inviscid fluid. The problem is of both theoretical and practical interest in fluid mechanics research, given the role of such flows in water discharge measurements structures, underwater oceanic currents, river flows and shallow bar-built estuary inlets, among others. While three-dimensional computations are feasible, vertically averaged solutions are sought to gain efficiency. The vertically averaged representation of sill overflows based on the Serre–Green–Naghdi (SGN) theory is limited to very shallow flows, and a good averaged approach for large overflows is currently not available. High-level Green–Naghdi (GN) theory forms a hierarchy of theories of increasing accuracy based on expanding the kinematic field and vertically-averaging in a weighted-residual sense. These theories have been successfully applied to ocean research but so far, they have not been applied to flow in open channels and structures. In this work, the high-level Green–Naghdi theories, of which SGN equations are the lowest level possible (GN level I theory), are formulated and newly applied to the sill-controlled flow problem. High-level GN theory is compared with detailed experiments from the literature and new ones conducted, and with a new fully non-linear vertically resolved potential flow solver which uses a  $x-\psi$  mapping. It was found that the GN expansions are convergent in the sill problem, in contrast to former perturbation solutions, which are asymptotic. The GN level V theory was found to be in good agreement with experiments for the sill-controlled flow problem, which excellently reproduced the free surface, bottom pressure, and vertical distributions of velocity and pressure. The GN level V theory was found to be applicable for relatively wide range of overflows up to  $E/R=3$ , where  $E$  is the minimum specific energy and  $R$  the sill crest radius of curvature. From a practical viewpoint, large improvements were observed when using GN level II theory, instead of GN level I (e.g. the SGN theory), producing good results up to  $E/R=1.75$ , which is the minimum level thus recommended in practice.

**Keywords** Critical flow · Obstacles · Green–Naghdi equations · Shallow water approximations

## 1 Introduction

The acceleration of a fluid layer over an obstacle in a stream produces at its crest the so-called control section or critical flow section, involving a transition from upstream subcritical to downstream supercritical flow [46, 64]. This kind of flow is called sill-controlled, and it is theoretically a fundamental fluid mechanics problem [70, 71, 82]. The sill-controlled flow problem is also important in practice given its use for water discharge measurement in free surface flows [59, 71], its role in underwater flow over oceanic sill and straits [28, 30], and in flows over boulders in a river stream. It is also an important mechanism to limit the propagation of infragravity waves from the ocean into the river across the inlet of shallow estuaries [2, 92].

The sill-controlled flow is well characterized by the Euler equations for an inviscid fluid assuming irrotational flow, thus critical flow is essentially an irrotational flow problem [31, 67–71]. However, the simple hydrostatic equations and linked critical flow theory [46] cannot be applied when streamlines are curved and sloped at the control sections, e.g., for large overflows in a sill [19]. In these cases, a solution from the Euler equations is needed, either using a vertically resolved model or an approximate vertically averaged one with enough vertical resolution incorporated. One of such methods is the critical flow theory of Fawer [31], which permits to compute the discharge characteristics of control sections at large overflows based on an interpolation formula for the streamline curvature at the sill crest, to be fitted to flow net results. However, the method is semi-empirical, and resorts to experiments or to a full two-dimensional flow net are required for calibration. Furthermore, only crest quantities are determined [11]. A different path is to solve the full boundary value problem instead of conducting critical flow computations at the sill crest. Dai and Sheng [23] reviewed the performance of the three main modeling approximations used for the full solution of sill overflows: The Reynolds-Averaged Navier Stokes (RANS) equations, which is a vertically resolved turbulent model, and two vertically averaged models, the Saint-Venant hydrostatic equations (SWE), and the Serre–Green–Naghdi equations (SGNE). The SWE produced results identical to those of hydrostatic critical flow theory at a weir crest [14], and non-hydrostatic effects are therefore not handled. The Serre–Green–Naghdi theory was developed for ocean dynamics [38, 39, 73, 80], and it is a depth-averaged fully non-linear and weakly dispersive non-hydrostatic Boussinesq type model recently applied to open channel flows [6, 7]. There is no calibration parameter in this theory, and the full solution along the obstacle is generated from it. However, it can only be applied to shallow flows [15]. Turbulence and vorticity are in general small in sill overflows without hydraulic jumps at the lee side [17, 31, 84]. Therefore, a reference vertically resolved model for the sill-controlled flow problem consists in Laplace equations for the stream and potential functions forming the flow net [53, 71] and Bernoulli equation for the free surface streamline [22, 56], instead of the RANS equations. The consequence is that a vertically resolved solution constructing a flow net numerically is feasible, but none of the available vertically-averaged models, namely the SWE or the SGNE, are good models for large sill overflows.

Given the theoretical and practical importance of the sill-controlled flow, and the lack of a robust vertically-averaged model to deal with it with generally, this research focus on exploring an alternative path to its modeling. The Serre–Green–Naghdi theory is the lowest level of approximation in a hierarchy of approximate theories, of increasing complexities, proposed by Green and Naghdi [38–42] and Green et al. [37]. These are called Green–Naghdi (GN) theories, and the lowest level is called GN I theory

[75], which is equivalent to the SGN theory. The method consists in producing an approximate representation of the vertical structure of the flow and uses it to develop integrated models where the dependence on the vertical coordinate is removed. Each level of the theory is classified according to the expansion adopted for the kinematic field. For level I, the horizontal velocity is constant with elevation whereas, for level II, it is linear, for level III cubic, for level IV quartic, and so on... Increasing the level of the theory the vertical resolution of the theory increases.

The original presentation of the theory by Green and Naghdi in their “directed fluid sheets” papers was tedious and difficult to follow, given its continuum mechanics nomenclature and formulation, more familiar to elasticity problems [60]. Shields and Webster [75] deserve the full credit for having reworked it in a fashion related to fluid mechanics problems. They used a variational approach due to Kantorovich and Krylov [48] which allowed a systematic development of the high levels of the theory. The same method was essentially applied by Steffler and Jin [78]. High-level GN theory has been successfully used in ocean dynamics problems [26, 27, 29, 74, 75, 85–88, 90, 91, 94–99], and it has been demonstrated in those works that increasing the level of the theory allows to obtain greater accuracy results. For river hydraulics, a theory similar to GN II level was developed by Steffler and Jin [78] and subsequently applied [8–10, 34–36, 50, 51]. So far, high-level GN theory was only applied to water waves problems.

Naghdi et al. applied first the GN theory to steady flows over channel structures, and used the low order GN level I theory in the flow at a free overfall [61, 63], flow over a sill [64], flow past a sluice gate [65], flow over a step [66] and the transition to planing of a boat [62]. Webster and Zhang [89] determined, using GN I theory, the steady approaching flow and free jet at free overfalls ending with ramps, given its relation to plunging breaker flows, and concluded that progress involved future application of a GN II high level theory. Thus, so far only the low level GN I theory was applied to flow in channel structures.

Perturbation methods [5, 83] can alternatively be applied to investigate the sill overflow problem. This was done by Castro-Organ et al. [16], who found a solution using as shallowness parameter  $\varepsilon$  the ratio of specific energy  $E$  to crest radius of curvature  $R$  at the sill crest. The series were found to be asymptotic, thus the solution limited to  $\varepsilon = E/R < 1$ . Given that the perturbation solution cannot be applied to large overflows by increasing the order of the expansions, it is relevant to investigate if the Green–Naghdi expansions are convergent in the sill flow problem and compare the results to the shallow water expansions.

The main objective of the work is therefore to develop high-level Green–Naghdi theories and apply them to the sill-controlled flow problem. Several options are possible to formulate the variational problem. In this paper, we generate high-level Green–Naghdi equations following an earlier method by Levich and Krylov [52], applied by Zhang et al. [93] to water waves problems. The variational GN equations are then used to simulate sill-controlled flows, including free surface and bottom pressure profiles, velocity and pressure distributions at the minimum specific energy section and the discharge characteristics for high-head overflows. Results are compared to several experimental datasets available in the literature and with new experiments conducted in a large-scale asymmetric bed sill involving a large curvature variation. The GN theory is further compared to a new full two-dimensional solution specifically constructed for this research, and its limitations are discussed.

## 2 Green–Naghdi modeling of free surface flow

### 2.1 The Levich–Krylov method

Let us consider the Euler equations for flows over an uneven and rigid bed (Fig. 1) [82] stating conservation of mass and momentum in the horizontal and vertical directions as follows:

$$\frac{\partial u}{\partial x} + \frac{\partial w}{\partial z} = 0, \quad (1)$$

$$\frac{\partial u}{\partial t} + \frac{\partial u^2}{\partial x} + \frac{\partial uw}{\partial z} + \frac{1}{\rho} \frac{\partial p}{\partial x} = 0, \quad (2)$$

$$\frac{\partial w}{\partial t} + \frac{\partial uw}{\partial x} + \frac{\partial w^2}{\partial z} + \frac{1}{\rho} \frac{\partial p}{\partial z} + g = 0. \quad (3)$$

here  $u$  and  $w$  are the velocity components in the  $x$  (horizontal) and  $z$  (vertical) directions, respectively;  $p$  is water pressure;  $g$  the gravity acceleration; and  $t$  is time. The kinematic boundary conditions at the free surface (subscript  $s$ ) and bed (subscript  $b$ ), are

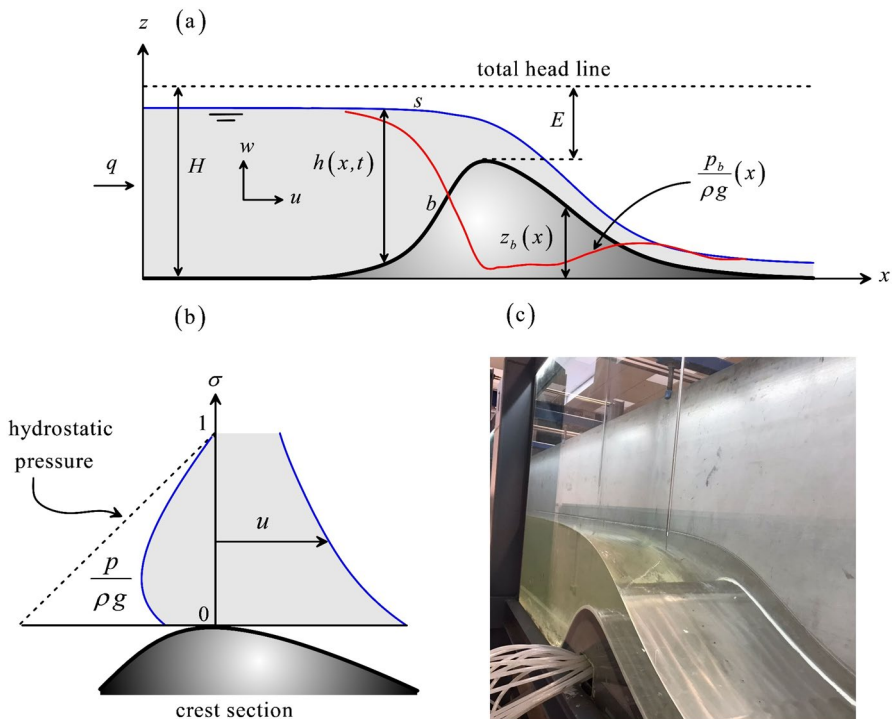


**Fig. 1** Definition sketch **a** Flow over a sill, **b** crest horizontal velocity and pressure distributions, **c** typical view of laboratory model test at the University of Córdoba

$$w_s = \frac{\partial h}{\partial t} + u_s \frac{\partial z_s}{\partial x}, \tag{4}$$

$$w_b = u_b \frac{\partial z_b}{\partial x}. \tag{5}$$

where  $h(x, t)$  is the water depth and  $z_b(x)$  the bed elevation. At the free surface, the dynamic boundary condition is  $p_s=0$ . The full problem resolved by Eqs. (1)–(5) is supplemented with initial and boundary conditions for solution.

We seek an approximate solution to the full problem given by Eqs. (1)–(5) by applying the Green Naghdi theory to the sill-controlled flow problem of Fig. 1. The problem formulation is treated as an unsteady flow for generality, although some intrinsic unsteady flow limitations are discussed later, given that this research focusses on steady flow solutions. The main ingredient of Green Naghdi theory consists in expanding the velocity using a set of base functions depending on the vertical coordinate, and then finding a solution “satisfied at large” [75], e.g., in a weighted-residual sense, much similar in nature to the method of finite elements in numerical analysis [32, 33]. However, here the expansions are used to remove a dimensional coordinate from the problem (in our case the elevation  $z$ ) instead of producing algebraical system of equations.

Green–Naghdi type modeling approximations can be derived following several tough related methods, like those presented by Shields and Webster [75] and Steffler and Jin [78], see also Castro-Orgaz et al. [18] for a detailed review. Here we will follow the Levich and Krylov’s [52] earlier method, given that the analytical work is straightforward. This method has been applied to water waves problems by Zhang et al. [93], who called it Boussinesq–Green–Naghdi rotational water wave theory, but it has so far not been applied to flow in channel structures. The Green Naghdi theory starts by assuming that the horizontal velocity  $u$  admits an expansion of the type [48, 52, 75, 78]

$$u(x, t, z) = u_0(x, t) + \sum_{j=1}^N u_j(x, t)\phi_j(\sigma), \quad \sigma(x, z, t) = \frac{z - z_b(x)}{h(x, t)}, \tag{6}$$

where the velocity coefficients  $u_0, u_1, u_2, \dots$  are functions of  $(x, t)$  but not of elevation  $z$ , and  $\phi_j$  is a set of base functions, which by choice are functions of the sigma coordinate  $\sigma$  only, which varies from zero at the channel bottom to unity at the free surface. Of course, this dependence is arbitrary, and the base functions may be directly functions of the elevation  $z$ , e.g. as done by Demirbilek and Webster [26, 27] and Webster et al. [91]. Here, we select for  $\phi_j$  an orthogonal base given by the shifted Legendre polynomials following Steffler and Jin [78], which are determined by Rodrigues’ formula [1]

$$\phi_j = \frac{1}{j!} \frac{d^j}{d\sigma^j} \left[ (\sigma - \sigma^2)^j \right]. \tag{7}$$

Use of this orthogonal base simplifies the analytical work given the cancellation of several integrals of the ensuing theory. The polynomials up to  $j=4$  are

$$\phi_0 = 1, \tag{8}$$

$$\phi_1 = 1 - 2\sigma, \tag{9}$$

$$\phi_2 = 1 - 6\sigma + 6\sigma^2, \tag{10}$$

$$\phi_3 = 1 - 12\sigma + 30\sigma^2 - 20\sigma^3, \tag{11}$$

$$\phi_4 = 1 - 20\sigma + 90\sigma^2 - 140\sigma^3 + 70\sigma^4, \tag{12}$$

which are plotted in Fig. 2.

The integrals of these functions from 0 to 1 with respect to the sigma coordinate are null, except that for  $\phi_0$ . Thus, integration of Eq. (6) across the flow depth to compute the unit discharge  $q$  produces  $q = u_0 h$ , e.g., the coefficient  $u_0$  is the depth-averaged velocity. This is different from Demirbilek and Webster [26, 27], as their  $u_0$  coefficient is not the depth-averaged velocity given that the base functions they selected is the sequence  $z, z^2, z^3, z^4, \dots$ . In our method,  $u_0$  has directly a physical meaning. The expansion given by Eq. (6) is to be used in Eqs. (1)-(5). Still, a closure for  $w$  and  $p$  is needed in these equations. Following Levich and Krylow [52], the  $w$ -closure is found by vertical integration of Eq. (1), resulting [13]

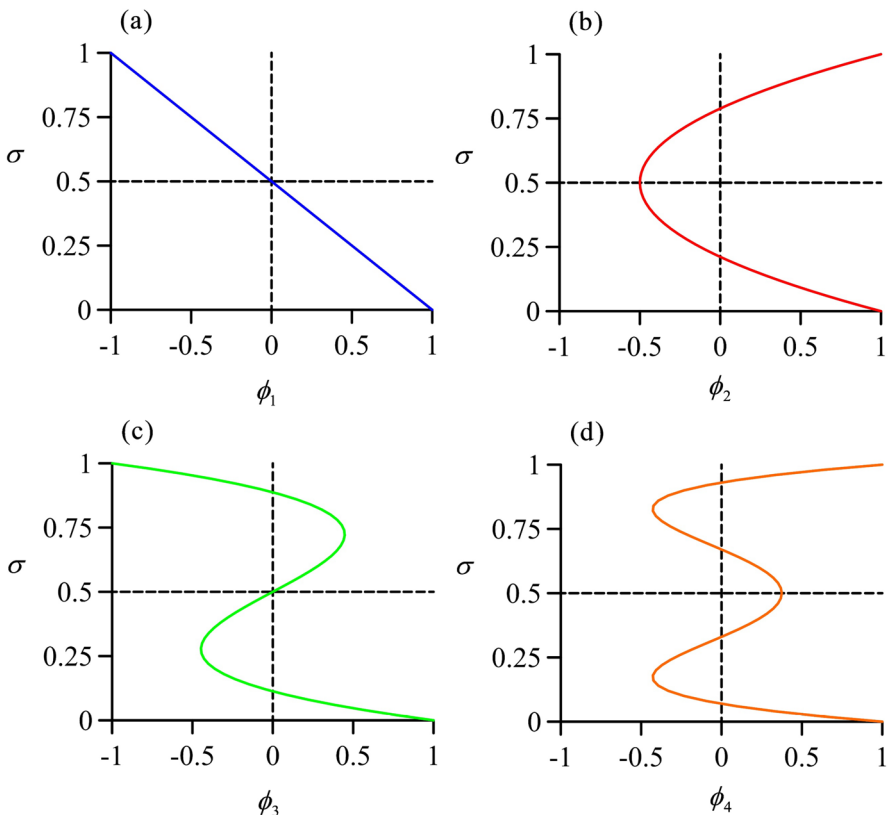


Fig. 2 Legendre shifted orthogonal base using sigma coordinate

$$w(x, z, t) = w_b - \int_{z_b}^z \frac{\partial u}{\partial x} dz. \tag{13}$$

Inserting Eqs. (5) and (6) into Eq. (13), an expression for  $w$  follows, which is a  $N + 1$  degree polynomial. The pressure  $p$  is determined by vertical integration of the  $z$ -momentum balance [52], resulting from Eq. (3) setting  $p_s = 0$  [13]

$$p(x, z, t) = \rho g(z_s - z) + \rho(w_s^2 - w^2) + \rho \int_z^{z_s} \frac{\partial w}{\partial t} dz + \rho \int_z^{z_s} \frac{\partial uw}{\partial x} dz. \tag{14}$$

The function to model  $p$  is found by inserting the expansion for  $u$  and the approximation for  $w$  obtained from Eq. (13), resulting a  $2N + 2$  degree polynomial. The solution of the problem requires the computation of  $h(x, t), u_0(x, t), u_1(x, t), \dots, u_N(x, t)$ , e.g., there are  $N + 1$  unknowns, and the same number of equations is therefore needed. The system of equations needed is obtained by using variational statements, as is explained in the next section.

In the application of Zhang et al. [93] to water waves problems, a Boussinesq scaling is used to truncate the polynomial expansions for  $w$  and  $p$  obtained from Eqs. (13) and (14). In our developments, no scaling was used and all the terms of the  $(u, w, p)$  expansions are retained, as is done also in Shields and Webster (1998) and Steffler and Jin [78].

### 2.2 High-level variational systems of equations

An exact equation of this theory is the vertically integrated mass conservation statement

$$\frac{\partial h}{\partial t} + \frac{\partial q}{\partial x} = 0, \tag{15}$$

obtained by vertical integration of Eq. (1) upon using Eqs. (4) and (6). Equation (15) is an evolution relation that produces a closure for  $h(x, t)$ . Now, the determination of the  $u_j$  coefficients is done by resorting to the following variational statements obtainable from the  $x$ -momentum balance:

$$\int_{z_b}^{z_s} \phi_j \left( \frac{\partial u}{\partial t} + \frac{\partial u^2}{\partial x} + \frac{\partial uw}{\partial z} + \frac{1}{\rho} \frac{\partial p}{\partial x} \right) dz = 0. \quad j = 0, 1, 2, \dots, N \tag{16}$$

Inserting the expansions for  $(u, w, p)$  into Eq. (16) and conducting the corresponding differentiations and integrals, a system of  $N$  equations follows, one for each different  $\phi_j$  used. Here, the weights are taken equal to the base functions, thus it is a Galerkin procedure [33].

Equation (16) is used thus to generate the  $N$  evolution equations for the unknown  $u_j$ 's. For  $N = 1$  the development can be done by hand, but for higher-level approximations the algebraical effort is formidable. In this work, the determination of  $w$  and  $p$  from Eqs. (13) and (14) and the variational system of equations from Eq. (16) was done with a symbolic algebra program, as done also by Shields and Webster [75]. The structure of the  $N$  mathematical Green–Naghdi equations obtained from Eq. (16) can be written in vector form as

$$\mathbf{A}\mathbf{f} + \mathbf{B}\frac{\partial\mathbf{f}}{\partial x} + \mathbf{C}\frac{\partial^2\mathbf{f}}{\partial x^2} = \mathbf{g}. \quad (17)$$

here  $\mathbf{A}$ ,  $\mathbf{B}$  and  $\mathbf{C}$  are  $N \times N$  matrices,  $\mathbf{g}$  is a vector of  $N$  dimension and  $\mathbf{f}$  is

$$\mathbf{f} = \frac{\partial\mathbf{u}}{\partial t}, \quad \mathbf{u} = \begin{pmatrix} u_0 \\ u_1 \\ u_2 \\ \vdots \\ u_N \end{pmatrix}. \quad (18)$$

Although the base used to expand  $u$  and the method to compute  $w$  and  $p$  used in this work are different from the choices by Demirbilek and Webster [26, 27], the mathematical structure of the ensuing high-level variational statements is the same, e.g. Equation (17). The Green–Naghdi equations are systems of coupled partial differential equations where the highest order of temporal differentiation in the ensuing mixed space–time derivatives of the  $u_j$  coefficients is one. What is different from one theory to another is the specific form of the elements of  $\mathbf{A}$ ,  $\mathbf{B}$ ,  $\mathbf{C}$  and  $\mathbf{g}$ . The matrices  $\mathbf{A}$ ,  $\mathbf{B}$ ,  $\mathbf{C}$  and vector  $\mathbf{g}$  contain only spatial derivatives, and the highest order of them is third. For  $N > 1$ , it is not only difficult to get the system (17) by hand computations, but also its statement in a document, given the extremely long expressions. For reference, we only give the results for  $N = 1$  in Appendix A. The symbolic program for the automatic generation of Eq. (17) is freely available upon request. In the current work, we have generated systems of Green–Naghdi (GN) equations for  $N = 0, 1, 2, 3$  and 4, which are called respectively GN I, GN II, GN III, GN IV and GN V. The case for  $N = 0$  implies  $u = u_0$ , which is the lowest level of the theory. It is coincident with the development of Serre [73], thus this model is commonly called Serre–Green–Naghdi theory, as previously commented.

### 2.3 Numerical method

The solution of the two-point boundary value problem in  $x$  and initial-value problem in  $t$  posed by Eq. (17) can be efficiently solved using the method developed by Demirbilek and Webster [26, 27]. Their numerical method consists basically in solving first the two-point boundary value problem and finds the vector  $\mathbf{f}$  at each node  $i$  of a finite-difference mesh on which the computational domain is discretized. Then, the  $\mathbf{u}$  vector at the new time level is determined by a time-stepping procedure of vector  $\mathbf{f}$ . The computer code developed for this work follows basically the same discretization and algorithms proposed by Demirbilek and Webster [26, 27] in the GNWAVE computer model. Some details of the solution algorithm are stated below for clarity.

We first consider the numerical approximation to Eq. (15), given that it can be solved independently to compute the water depth. We used upwind differencing for the continuity equation in our numerical model as follow

$$h(i)^{k+1} = h(i)^k - \frac{\Delta t}{2\Delta x} [3q(i) - 4q(i-1) + q(i-2)]. \quad (19)$$

where the index  $k$  is used to define the time level,  $\Delta x$  is the mesh spatial size and  $\Delta t$  is the time step. In the model by Demirbilek and Webster [26, 27], the continuity equation and the Green–Naghdi equations are both discretised using central in space and forward in time

finite-differences. For the test cases presented in the following sections no difference was found in the output of our solver using either a centered or an upwind discretization of the continuity equation. Moreover, both are equally simple to implement. As explained later, a smoothing filter is applied intermittently to  $h$  and  $\mathbf{u}$  to dampen the high frequency oscillations arising from finite-difference discretisation of the highly non-linear terms in GN models [95, 96]. If vertical accelerations are weak and pressure close to hydrostatic the model equations can be demonstrated to tend in the limit to the Saint Venant hydrostatic model [49]. For example, this would be the case for a very shallow overflow in Fig. 1, e.g., for  $E \rightarrow 0$ . A numerical solution of Saint Venant equations with a forward in time-centered in space scheme is unconditionally unstable [49]. Simply to avoid the possibility of having this potential source of instabilities, we used upwind differencing for the continuity equation. From a practical viewpoint, the filter makes the model robust and free of instabilities either using a centered or upwind differencing.

Now, returning to the Green–Naghdi Eq. (17),  $\partial \mathbf{f} / \partial x$  and  $\partial^2 \mathbf{f} / \partial x^2$  are discretized using second-order central finite differences, resulting the following discrete equations at node  $i$  of the mesh [26]

$$\begin{aligned} \tilde{\mathbf{A}}(i)\mathbf{f}(i-1) + \tilde{\mathbf{B}}(i)\mathbf{f}(i) + \tilde{\mathbf{D}}(i)\mathbf{f}(i+1) &= \mathbf{g}(i), \\ \tilde{\mathbf{A}}(i) &= \frac{\mathbf{C}(i)}{\Delta x^2} - \frac{\mathbf{B}(i)}{2\Delta x}, \\ \tilde{\mathbf{B}}(i) &= -2\frac{\mathbf{C}(i)}{\Delta x^2} + \mathbf{A}(i), \\ \tilde{\mathbf{D}}(i) &= \frac{\mathbf{C}(i)}{\Delta x^2} + \frac{\mathbf{B}(i)}{2\Delta x}. \end{aligned} \tag{20}$$

The matrices  $\mathbf{A}(i)$ ,  $\mathbf{B}(i)$ ,  $\mathbf{C}(i)$  and vector  $\mathbf{g}(i)$  contain up to third-order spatial derivatives of  $h(x, t)$ ,  $z_b(x)$  and vector  $\mathbf{u}(x, t)$  at node  $i$ . These derivatives are all discretized using second-order central finite-differences. Once this discretization is accomplished, the problem solution consists in finding  $\mathbf{f}(i)$  subject to the boundary conditions at the inflow and outflow sections. Demirbilek and Webster [26] developed a very smart and efficient generalization of the Thomas algorithm for solving the block-tridiagonal system posed by Eqs. (20), which we used here. Once the vector  $\mathbf{f}(i)$  is available for all the computational nodes, the vector  $\mathbf{u}$  is determined at next time level from

$$\mathbf{u}(i)^{k+1} = \mathbf{u}(i)^k + \mathbf{f}(i)^k \Delta t. \tag{21}$$

The values obtained for  $h$  and  $\mathbf{u}$  are used to solve again Eq. (20) and get an estimation of  $\mathbf{f}$  at time level  $k+1$ . A better estimation of  $\mathbf{u}$  at  $k+1$  is then using the trapezoidal rule

$$\mathbf{u}(i)^{k+1} = \mathbf{u}(i)^k + \frac{1}{2} [\mathbf{f}(i)^k + \mathbf{f}(i)^{k+1}] \Delta t. \tag{22}$$

Now we describe the initial and boundary conditions used to simulate the overflow problem of Fig. 1, where a discharge  $q$  enters in the flume, spills over the sill and freely leaves the computational domain at the outlet. At the inlet section, we set  $u_0$  to a specified value which is kept constant during all the transient flow, and set to zero the remaining components of vector  $\mathbf{u}$ . The water depth at the inlet section at any instant is found by a zero-order extrapolation of the actual interior solution. Vector  $\mathbf{f}$  at the inlet section is set to zero, given that none of the  $\mathbf{u}$  components will be a time-varying quantity. The outlet open section with freely leaving waves is modeled for  $h$  and  $\mathbf{u}$  solving the advection equations

$\partial h/\partial t + c \partial h/\partial x = 0$  and  $\partial \mathbf{u}/\partial t + c \partial \mathbf{u}/\partial x = 0$  with the celerity estimated as  $c = (gh)^{1/2}$  [74]. The vector  $\mathbf{f}$  is updated in time at the outlet using Euler backward formula. The initial free surface profile corresponds to a hydrostatic transcritical flow profile over the sill obtained by inversion of the specific energy (energy divided per specific weight of fluid, the dimension of which is a length scale) for hydrostatic flows  $E(x) = H - z_b(x) = h + q^2/(2gh^2)$  [46]. Once this initial profile is set and the inlet–outlet conditions are specified, a time-dependent flow adjustment develops over the sill until a steady flow condition is achieved. For the transient computations,  $\Delta t$  is kept small to avoid stability problems, with its value fixed by trial-and-error numerical experiments, given the lack of a stability analysis for the complex Green–Naghdi equations. A Savitzky–Golay smoothing filter is applied intermittently each 10-to-20-time steps to  $h$  and  $\mathbf{u}$  to dampen the high frequency oscillations arising from finite-difference discretization of the highly non-linear terms in GN models [95, 96], as well as those generated at the inlet and outlet boundaries [26]. The steady flow solutions generated with the unsteady GN I model were compared to the implicit steady finite-difference solver for these equations developed by Castro-Orgaz et al. [15], resulting imperceptible differences, confirming that the smoothing filter had a negligible effect on the physical solutions seek in this work.

### 3 Fully non-linear potential flow modeling

In this section, a new model for determining the irrotational flow pattern over a sill is presented. It consists in combining an  $x$ - $\psi$  mapping of Laplace equation for the interior flow field with a new iteration of the non-linear free surface boundary condition posed by Bernoulli equation. The new iteration scheme consists in: (i) using an accurate initial free surface position based on the GN V solution, (ii) setting limits to the free surface corrections based on the analysis of the discrete-Bernoulli diagram upstream of the weir crest, and (iii) iterating the upstream water depth (and hence the Bernoulli constant) using a control volume momentum balance.

#### 3.1 The $x$ - $\psi$ mapping

The Green–Naghdi Eq. (17) approximates the original system of Euler equations, where irrotationality was not imposed. However, it was demonstrated by Webster and Shields [85] that, as the level of the theory increases, e.g. as  $N$  increases, the solution tends to be that for an irrotational flow, if vorticity is not introduced in the flow domain. The flow over a sill can be nicely modeled as an irrotational flow motion [31, 84] and, for this reason, a fully non-linear potential flow solver was developed for comparison purposes with the Green Naghdi solutions. In the present work, we employ the so-called  $x$ - $\psi$  mapping, where  $\psi$  is the stream function. Using this mapping, the elevation is taken as a dependent variable of  $x$  and  $\psi$ , resulting the Laplacian [4, 56–58]

$$\nabla^2 z = \frac{\partial^2 z}{\partial x^2} \left( \frac{\partial z}{\partial \psi} \right)^2 + \frac{\partial^2 z}{\partial \psi^2} \left[ 1 + \left( \frac{\partial z}{\partial x} \right)^2 \right] - 2 \frac{\partial^2 z}{\partial x \partial \psi} \frac{\partial z}{\partial x} \frac{\partial z}{\partial \psi} = 0. \quad (23)$$

The solution of this elliptic problem yields for a given value of  $\psi$  the coordinates of a streamline. The velocity components ( $u, w$ ) in the directions ( $x, z$ ) are determined from

$$u = \frac{\partial \psi}{\partial z}, \tag{24}$$

$$w = u \frac{\partial z}{\partial x}. \tag{25}$$

At the free surface  $\psi=q$  and the position of this streamline shall be determined as part of the problem solution. At the bottom  $\psi=0$  and the bottom streamline  $z(x, \psi=0)=z_b(x)$  is known. At the inflow and outflow sections, the velocity  $u$  is uniform with elevation and the pressure hydrostatic, implying a linear variation of  $z$  with  $\psi$ . At the free surface Bernoulli equation yields a non-linear boundary condition to be satisfied by this specific streamline, namely  $H=z_s + (u_s^2 + w_s^2)/(2g)$ , where  $H$  is the Bernoulli constant. The free surface streamline  $z_s(x)=z(x, \psi=q)$  shall verify this complex non-linear boundary condition, which is difficult to satisfy in a numerical setting, as discussed below. In the sill controlled or critical flow problem either  $H$  is known, and  $q$  shall be determined as part of the solution or equivalently,  $q$  is known, and  $H$  is to be determined [24, 25, 43, 47]. The last case is the most common, and it is the situation considered in this work [22].

### 3.2 Numerical method

The numerical solution consists in three nested iteration loops to determine the position of the interior streamlines, the position of the free surface streamline and the upstream water depth.

#### 3.2.1 Iteration of interior streamlines

Let  $(i, j)$  be the node indices of a finite-difference mesh in the  $x$ -direction and  $\psi$ -directions, the derivatives appearing in the Laplacian are estimated with second-order accuracy as

$$\frac{\partial z}{\partial x} = \frac{z(i+1, j) - z(i-1, j)}{2\Delta x}, \tag{26}$$

$$\frac{\partial z}{\partial \psi} = \frac{z(i, j+1) - z(i, j-1)}{2\Delta \psi}, \tag{27}$$

$$\frac{\partial^2 z}{\partial x^2} = \frac{z(i+1, j) - 2z(i, j) + z(i-1, j)}{(\Delta x)^2}, \tag{28}$$

$$\frac{\partial^2 z}{\partial \psi^2} = \frac{z(i, j+1) - 2z(i, j) + z(i, j-1)}{(\Delta \psi)^2}, \tag{29}$$

$$\frac{\partial^2 z}{\partial x \partial \psi} = \frac{z(i+1, j+1) - z(i-1, j+1) - z(i+1, j-1) + z(i-1, j-1)}{4\Delta x \Delta \psi}. \tag{30}$$

Inserting Eqs. (26)–(30) into Eq. (23) produces an algebraic system of linear equations, which is solved herein by a successive over-relaxation method [49] with an over-relaxation coefficient of 1.8. Once the solution converged, the elevation at each node of the mesh is available, e.g., the discrete version of the streamlines. The velocity components are thus given by

$$u(i, j) = \frac{2\Delta\psi}{z(i, j+1) - z(i, j-1)}, \quad (31)$$

$$w(i, j) = u(i, j) \frac{z(i+1, j) - z(i-1, j)}{2\Delta x}. \quad (32)$$

The  $u$ -velocity at the free surface ( $j=M$ ) and bottom ( $j=1$ ) are determined from

$$u_s = u(i, M) = \frac{2\Delta\psi}{3z(i, M) - 4z(i, M-1) + z(i, M-2)}, \quad (33)$$

$$u_b = u(i, 1) = \frac{2\Delta\psi}{-3z(i, 1) + 4z(i, 2) - z(i, 3)}. \quad (34)$$

### 3.2.2 Iteration of free surface streamline

For a unit discharge  $q$ , the actual target energy head is determined using the upstream water depth at the inlet section  $h_u$  as  $H = h_u + q^2/(2gh_u^2)$ . Given an actual position of the free surface streamline  $z_s(x)$ , the energy head at the free surface for a generic section at distance  $x$  may be obtained as

$$H(x) = z_s + \frac{u_s^2}{2g} \left[ 1 + \left( \frac{\partial z_s}{\partial x} \right)^2 \right]. \quad (35)$$

If this position for the free surface is incorrect, an energy residual  $e(x) = H(x) - H$  results at that section, with  $H$  as the energy head or Bernoulli constant of the problem. It implies that the pressure at the free surface is not zero, violating the dynamic boundary condition. An iteration process to find a correct estimation of the free surface position is, therefore, needed [79]. The iteration process for the sill problem is not simple, and, thus, it was found in this work necessary to modify the original algorithm proposed by Montes [56–58] to allow computation of large overflows. Montes [56, 57] proposed an iteration method where the coordinate of each free surface node was adjusted independently. This approach diverges for large overflows and the method proposed by Cheng et al. [22] was found to be more adequate, thus it was adapted to our numerical implementation. Here, the coordinate of each free surface node between the inlet and outlet sections is adjusted implicitly by using the Newton–Raphson method as follow

$$\mathbf{z}_s^{s+1} = \mathbf{z}_s^s + \Delta \mathbf{z}_s, \quad (36)$$

$$\Delta \mathbf{z}_s = -\mathbf{J}^{-1} \mathbf{e}, \quad (37)$$

where  $s$  is the iteration index,  $\Delta \mathbf{z}_s$  the correction vector and  $\mathbf{J}$  the Jacobian matrix. Even using this implicit implementation, the solution is complex, and care is needed while applying Eq. (36) to iterate the free surface position [79]. Cheng et al. [22] and Montes [56] indicated that, upstream of the sill crest, there is a zone of uncertainty where changes in  $H$  produces maximal free surface corrections, or inversely, where a change in the free surface has a negligible effect in the Bernoulli constant. In practice, this is traduced to two practical rules [22]: (i) first, a damping shall be applied to the corrections obtained from Eq. (37), ensuring that the free surface experiences small movements during each iteration; and (ii) second, limits shall be set when moving the free surface to ensure corrections are always reasonable. To our knowledge, neither the reason for this behaviour upstream of the sill crest nor how to set reasonable limits for iteration were so far explained in the literature. The discrete version of the Bernoulli Eq. (35) has been analysed in Appendix B, thereby explaining the anomalous behaviour upstream of the sill crest and how to set reasonable iteration limits. A linked consequence is that the initial position of the free surface streamline cannot be arbitrary, but a good approximation. We have used in this work as initial free surface streamline the flow profile generated with the GN V model.

To determine the correction vector  $\Delta \mathbf{z}_s$ , it is necessary to construct the Jacobian matrix. We have followed the procedure suggested by Cheng et al. [22] and determined it numerically as follows. Given that all free surface nodes are interrelated, a change in  $H$  at a node affects all the remaining free surface nodes. Therefore, the change in the Bernoulli constant at all nodes is determined by displacing the free surface position at a node a small magnitude  $\Delta p$  from the actual solution. A full solution of the Laplacian field is required to compute  $H$  at all the free surface nodes after this local displacement. This procedure is repeated displacing all the free surface nodes twice, once using a forward displacement and another using a backward displacement. The Jacobian matrix elements are thus determined as

$$J(i, j) = \frac{\partial H(i, j)}{\partial z_s(j)} \approx \frac{H_f(i, j) - H_b(i, j)}{2\Delta p} \tag{38}$$

where  $H_f(i, j)$  is the energy head at node  $i$  displacing the surface position at node  $j$  to  $z_s(j) + \Delta p$  and  $H_b(i, j)$  is the energy head at node  $i$  displacing the surface position at node  $j$  to  $z_s(j) - \Delta p$ . Iterations are stopped when the average pressure head on the free surface is in absolute value down a tolerance, typically 0.1 mm. The free surface dynamic boundary condition was satisfied with 15–25 iterations.

### 3.2.3 Iteration of upstream water depth

A control volume with boundary sections consisting of the inlet and the sill crest is considered to establish an integral momentum balance. The momentum balance for the control volume is used to check the accuracy of the numerical solution and iterate the upstream water depth  $h_u$  if necessary.

The streamwise momentum equation for sill problem is [64]

$$\frac{d}{dx} \int_{z_b}^{z_s} \left( \frac{p}{\rho g} + \frac{u^2}{g} \right) dz = - \frac{\partial z_b}{\partial x} \frac{p_b}{\rho g}, \tag{39}$$

which, integrated between the upstream section  $u$  and the crest section  $cr$ , yields the control volume balance

$$S_u = D + S_{cr}. \quad (40)$$

Here  $D$  is the drag force per unit width over the obstacle up to the crest [64, 65], and  $S$  the momentum function

$$S = \int_{z_b}^{z_s} \left( \frac{p}{\rho g} + \frac{u^2}{g} \right) dz. \quad (41)$$

After convergence of the free surface position, the different terms in Eq. (40) are numerically evaluated using the 2D results, and a momentum deficit or excess  $\Delta M$  results

$$\Delta M = S_u - (D + S_{cr}). \quad (42)$$

The upstream water depth  $h_u$  can be thus changed to seek a solution with  $\Delta M=0$ . Keeping  $D$  and  $S_{cr}$  constants, an approximate correction equation to use in the Newton–Raphson method is

$$\Delta h_u = - \frac{\Delta M}{h_u \left( 1 - \frac{q^2}{gh_u^3} \right)}. \quad (43)$$

The target energy head is recomputed after each iteration of the upstream water depth. Two or three iterations were typically enough to get accurate results.

## 4 Results

The correct method to apply GN theory and find a converged solution is to compare the GN models of different levels, increasing the levels until the results do not change. This is called self-convergence test of GN theory. Once a converged theory is determined their results can be compared to experiments and 2D irrotational flow solutions. This methodology was adopted in the following test cases, although we will also show how some intermediate theories compare with experiments and 2D solutions.

### 4.1 Flow profiles and crest distributions

Sivakumaran et al. [76] conducted experiments of sill-controlled flows in a horizontal flume, 0.915 m long, 0.65 m high and 0.30 m wide. Two kind of bed profiles were considered, symmetrical and asymmetrical. The experimental procedure and data are available in Sivakumaran [77], and these data were used here to test the accuracy of the different GN theoretical levels. The GN modelling was accomplished using  $\Delta x=0.01$  m and  $\Delta t=0.001$  s to reduce truncation errors, although higher values could be used in some test. Figure 3 contains the experimental data corresponding to the flow over the asymmetrical bed profile designed using B-Splines [77]. The unit discharge for this test is  $q=0.11165$  m<sup>2</sup>/s, and the experimental free surface and bed pressure head profiles are plotted in Fig. 3. A first simulation using GN I theory was conducted, and it is included in the same figure, showing a systematic mismatch with experiments; the GN I theory predicts an unrealistic free surface blip in the crest zone. The results obtained with the 2D irrotational flow model using 20 streamlines are also presented to depict the free surface details at the crest zone

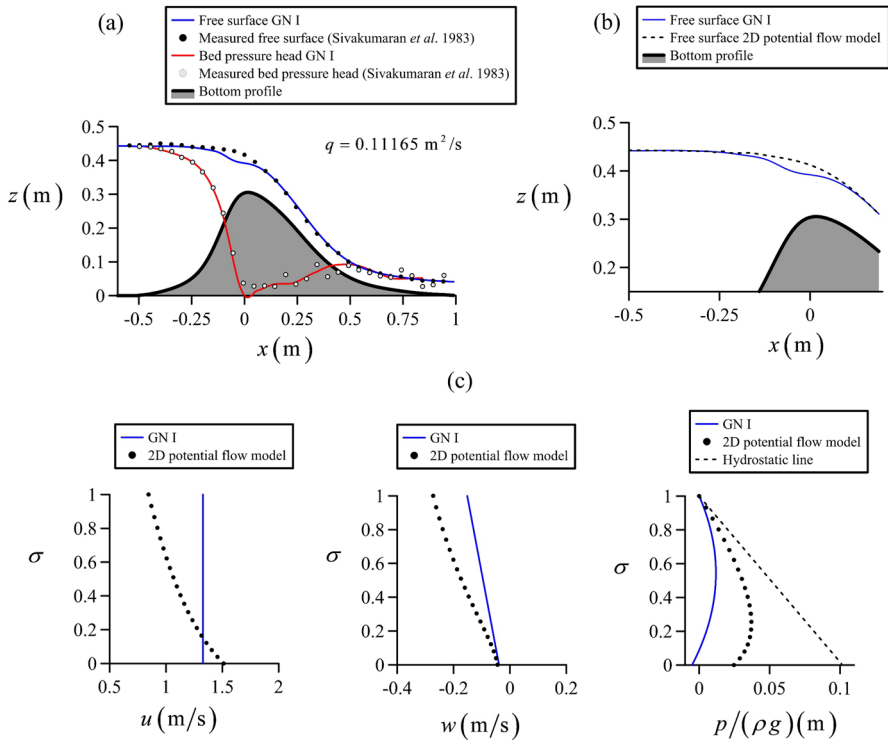


**Fig. 3** Flow over an asymmetrical bed profile: Comparison of GN I theory with experiments [77] and 2D irrotational flow results

and the deviations from GN I theory. The crest velocity and pressure distributions obtained with the 2D irrotational flow model are compared with those of GN I theory, showing again a systematic mismatch of the latter. The same test was run using the model constructed for GN II theory, and the results are plotted in Fig. 4 along with the experiments [77] and 2D irrotational flow results. Note the significant variation in the computed results using GN II instead of GN I theory; the predicted free surface and bed pressure profiles by the former theory are in excellent agreement with the experiments. A very small hump in the free surface is predicted by GN II at the crest, however. The crest velocity and pressure distributions predicted by GN II theory, though not perfect, are good approximations to the 2D flow results, and represent a significant improvement over the former GN I results. Finally, the same test is presented in Fig. 5 using the GN V theory. There is an excellent agreement of the GN V theory with the experiments. The 2D irrotational free surface and crest velocity and pressure distributions are as well excellently reproduced. For GN III and GN IV theories there are small variations, not presented here for brevity. Results from GN IV are indistinguishable from those of GN V, thus GN V is the converged theory for this test. The measured pressured head data by Sivakumaran [77] show oscillations not predicted by GN V theory. It is unknown if this is a limitation of the experimental measurements, or a feature not predicted by GN theory.

Figure 6 contains the experimental data corresponding to the flow over a symmetrical bed profile designed using a normal bell distribution of equation

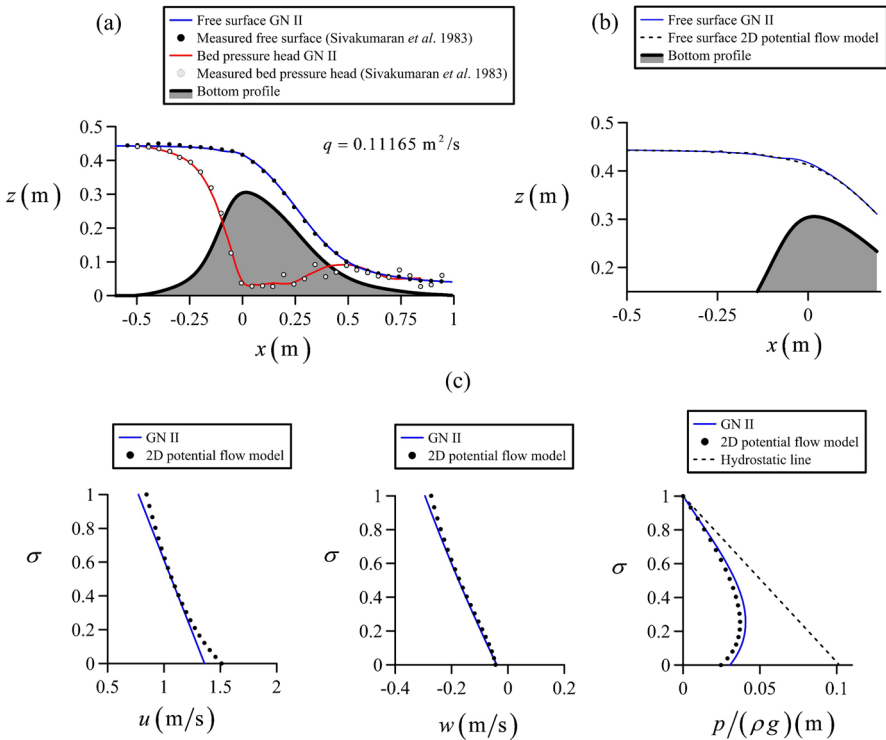


**Fig. 4** Flow over an asymmetrical bed profile: Comparison of GN II theory with experiments [77] and 2D irrotational flow results

$z_b = 0.2 \exp[-0.5(x/0.24)^2]$  (m) [77]. The unit discharge for this test is  $q = 0.1102 \text{ m}^2/\text{s}$ , and the experimental free surface and bed pressure head profiles are plotted in Fig. 6. The results of GN I theory included in the same figure are in this test a quite good approximation, albeit the upstream free surface level is clearly underpredicted. The predicted crest distributions for  $w$  and  $p$  are also a good approximation to the 2D results. The simulation of this test using GN II theory is plotted in Fig. 7, showing an excellent agreement with experiments and the 2D results, including the crest velocity and pressure distributions. Note that the crest distribution of  $u$  is in excellent agreement with the irrotational flow model, thereby suggesting that the crest velocity in this test is roughly linear. The use of higher-level theories produced results with minute variations from GN II theory, thus are not presented for brevity. For this test, GN II is the converged theory.

Flows over asymmetric bed profiles involving a strong variation of bed curvature are rare, with Sivakumaran’s [77] experiments presented in Fig. 5 as a notable exception. The B-spline bed profile constructed by Sivakumaran [77] produced some scatter in the measured bed pressures, however. It is unknown if this is related or not to the bed profile design using splines, possibly involving construction discontinuities in the bed high-order derivatives. To investigate the ability of GN theory to reproduce the bed pressure head in a zone of rapidly changing bed curvature, a new set of experiments were designed at the Hydraulics laboratory of the University of Córdoba, Spain. The

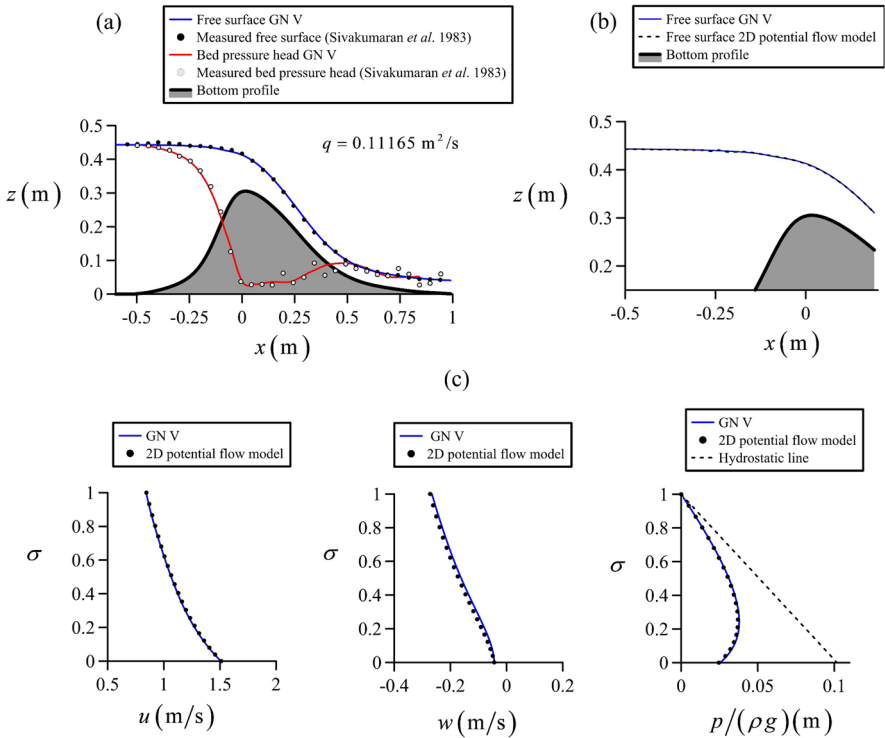


**Fig. 5** Flow over an asymmetrical bed profile: Comparison of GN V theory with experiments [77] and 2D irrotational flow results

laboratory is equipped with a 15 m long, 1 m high, 1 m wide tilting flume where a new obstacle of asymmetric shape was constructed using a log-normal profile of equation:

$$\begin{aligned}
 z_b &= z_{\text{top}} \exp \left[ -\frac{1}{2} \alpha (\ln X - \mu)^2 \right], \\
 X &= \frac{x}{L_{\text{obs}}} + \varepsilon, \\
 \varepsilon &= \exp \mu,
 \end{aligned}
 \tag{44}$$

where  $z_{\text{top}} = 0.21 \text{ m}$ ,  $\alpha = 3.7$ ,  $L = 0.68 \text{ m}$  and  $\mu = -0.6$  (Fig. 8a). This profile involves a strong variation of bed curvature, and it is a continuous curve for  $z_b$  as well as for  $dz_b/dx$ ,  $d^2z_b/dx^2$  and  $d^3z_b/dx^3$ , which are the derivatives appearing in GN theory at any level. Therefore, it is a well-suited test to check the performance of the GN theory without violation of any of the starting assumptions of this theory. Flow visualisation during the experiments was accomplished through the eight lateral transparent windows of 1.875 m width by 0.975 m height of the flume, with each window monitored by a camera perpendicularly installed in front of the flume, used to get the free surface profile. The discharge was supplied at the inlet of the flume regulating a valve. It was measured with an ultrasonic flowmeter of  $\pm 0.4\%$  accuracy installed in a recirculation pipe. Sixteen piezometric tubes were used to measure the bed pressure heads, with an estimated error of  $\pm 1 \text{ mm}$ .

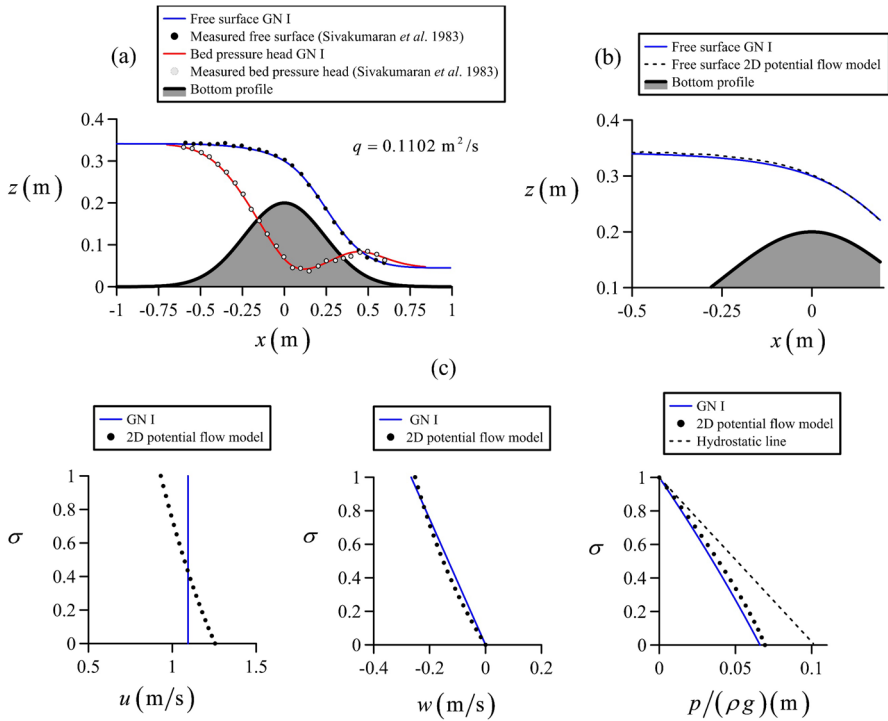


**Fig. 6** Flow over a symmetrical bed profile: Comparison of GN I theory with experiments [77] and 2D irrotational flow results

The experimental results for the free surface and bed pressure head profiles for a run with unit discharge  $q = 0.1637 \text{ m}^2/\text{s}$  are presented in Fig. 8 along with the simulation from GN V theory, showing an excellent agreement. The GN V theory is also in good agreement with the 2D potential flow results for this test, which are also included in the figure. The crest velocity and pressure distributions are predicted with good accuracy by GN theory. The measured and predicted bed pressures over the log-normal bed profile are both continuous, without any oscillations as previously reported by Sivakumaran [77]. Other runs conducted in the new experimental set-up produced similar results. Therefore, the modeling of bed pressures by GN V theory is in good agreement with experiments.

### 4.2 Discharge characteristics

The ability of GN theory at different levels to reproduce the discharge characteristics of obstacles is examined in this section. The discharge coefficient  $C_D$

$$C_D = \frac{q}{(gE^3)^{1/2}}, \tag{45}$$

of the low sill of Gaussian shape  $z_b = 0.2 \exp[-0.5(x/0.24)^2]$  [77] was determined with the GN I theory numerically, and the results are plotted in Fig. 9 versus the normalized specific

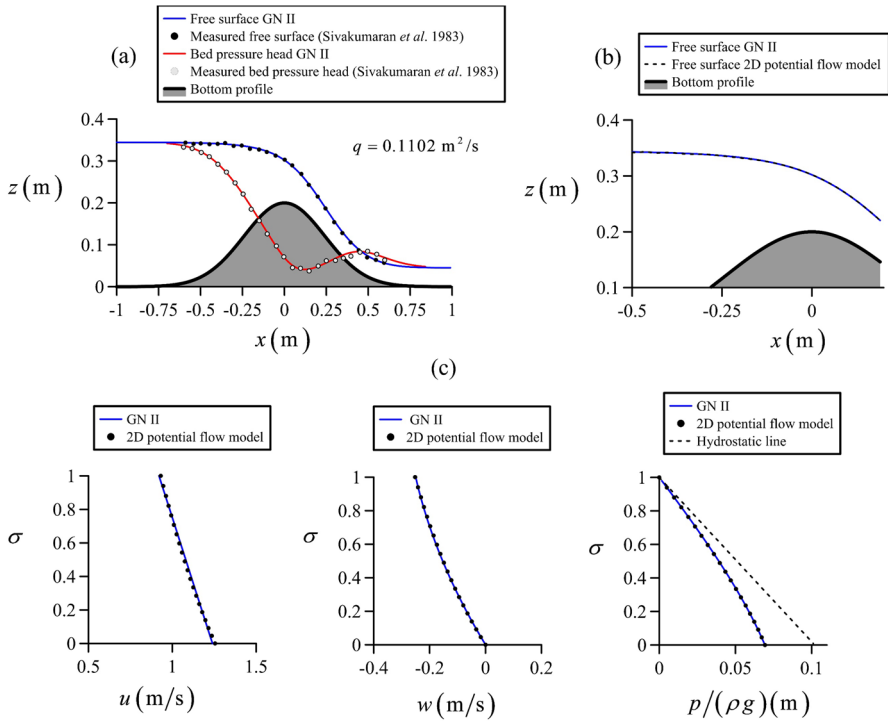


**Fig. 7** Flow over a symmetrical bed profile: Comparison of GN II theory with experiments [77] and 2D irrotational flow results

energy  $E/R$ , where  $R$  is the obstacle crest radius of curvature. Experiments of Castro-Orgaz [12] and Castro-Orgaz et al. [16] for low sills of circular and Gaussian shape are plotted in the same figure, along with the second order  $O(2)$  shallow water expansion [16, 54, 55]

$$C_D = \left(\frac{2}{3}\right)^{3/2} \left(1 + \frac{22}{81} \frac{E}{R}\right). \tag{46}$$

The shallow-water  $O(3)$  and  $O(5)$  expansions are also plotted in Fig. 9, but their coefficients are not stated here for brevity. These are available in Castro-Orgaz et al. [16]. The  $O(5)$  expansion is the optimally truncated series in the interval  $0 < E/R < 1$ , given that the shallow-water series were found to be asymptotic rather than convergent. Note that the GN I theory, which is equivalent to Serre–Green–Naghdi theory, is very close to the  $O(2)$  asymptotic expansion for  $E/R < 0.7$ , as previously found [15]. It does not closely match the experiments.

Results for the GN II theory are included in the same figure, showing a significant improvement over the GN I theory. This theory closely matches the experimental results up to  $E/R = 1$ , and it is also in very good agreement with the  $O(5)$  asymptotic expansion, which is the optimum result for this low sill test. The GN III theory produces imperceptible differences from GN II theory, we thus take GN II as the converged theory for the low sill test analyzed in Fig. 9.

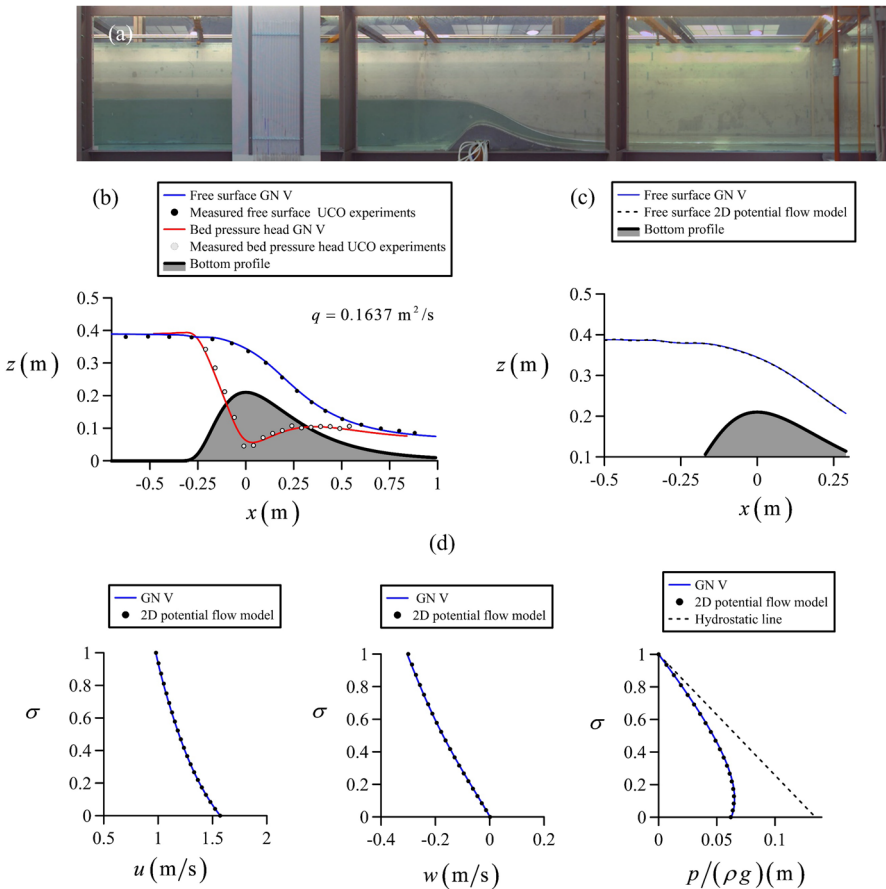
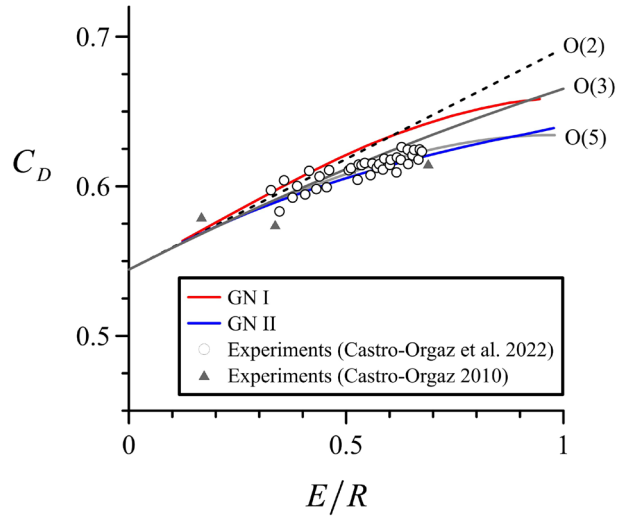


**Fig. 8** Flow over log-normal profile constructed for verification of GN V theory: Comparison with experiments and 2D irrotational flow results

A higher sill of Gaussian shape  $z_b = 0.6 \exp[-0.5(x/0.24)^2]$  was used to investigate the convergence properties of GN theory at higher levels of the theory, which are expected to be necessary for high-head overflows, e.g., for  $E/R > 1$ . The discharge coefficient for GN I, GN II, GN III, GN IV and GN V theories up to  $E/R = 3$  is plotted in Fig. 10a along with the 2D irrotational flow results and the O(2) and O(4) shallow water asymptotic expansions.

Figure 10a clearly shows that the shallow water expansions are asymptotic. We seek now to analyze the behavior of GN theory increasing its level from I to V. Results plotted in Fig. 10a reveal that GN I theory is not a good approximation at large heads, given the significant divergence from 2D results. For GN II theory, note that the accuracy increase over GN I theory is significant; the theory is in excellent agreement with 2D results up to  $E/R = 1.75$ , producing an overprediction of  $C_D$  onwards. This is a first remarkable result: the GN II theory is found again to be a significant improvement over GN I level. The GN III theory involves a notable variation over GN II theory at large heads. The GN IV level still produces a variation over GN III level, but variations in

**Fig. 9** Discharge characteristics of low height sill of Gaussian shape: Comparison of GN theory at different levels with experiments and shallow water asymptotic expansions



the results from GN IV to GN V level are however negligible and imperceptible visually. We thus take GN V level as the converged theory in this test. The second remarkable result is that the GN theory is found to be convergent by increasing the modeling level, e.g., the number of terms  $N$  in the  $u$ -series expansions. Deviations in the predicted  $C_D$  by GN V theory from 2D results are small, with a maximum deviation of 0.35% at  $E/R=3$ .

An example of self-convergence test for the free surface profiles is presented in Fig. 10b for  $q=0.3498 \text{ m}^2/\text{s}$ . Coordinates  $(C_d, E/R)$  for each GN level are also given in Fig. 10b. In line with Fig. 10a, a significant change in the predictions is observed from GN I to GN II. From GN IV to GN V, by contrast, results are almost identical; variations are in the 4th-decimal place for  $C_d$  and visually imperceptible in the flow profile. Therefore, for this test, GN V is adopted as the converged theory.

Based on Fig. 10, the predictions of GN V are better than those of GN I and GN II, as expected. Note, however, that the converged theory may be different for other sill-controlled flow tests. For the low sill simulated in Fig. 9, GN II theory was good enough. There may be cases demanding a level above V, e.g., VI or VII. This makes clear that, in any application of the GN theory, the self-convergence test is mandatory.

Now that GN V level is taken here as the practical model for sill-controlled flows; its accuracy is examined using experimental data of different sources, involving parabolic weirs [3], circular-crested weirs [12, 72, 84], Gaussian humps [76] and spillway profiles [31, 45]. The  $C_D$  curve modeled by GN V theory is compared in Fig. 11 with these datasets, and the O(2) leading order shallow water expansion is included for reference at low heads. The results of GN V theory are found to be in good agreement with experiments up to the large head  $E/R=3$ . For low heads, e.g.,  $E/R < 0.5$ , it overlaps with the O(2) shallow-water expansion, as expected.

The flow over a sill crest is frequently accomplished using critical flow computations including the effects of streamline curvature at the obstacle crest [11, 19, 31]. A theory which allows such computations is that of Fawer [11, 31], where the streamline curvature is assumed to obey the following interpolation formula at the crest

**Fig. 10 a** Convergence features of discharge characteristics at higher-levels of the Green–Naghdi theory; comparison with shallow water asymptotic expansions and 2D irrotational flow results; **b** self-convergence test for free surface profile

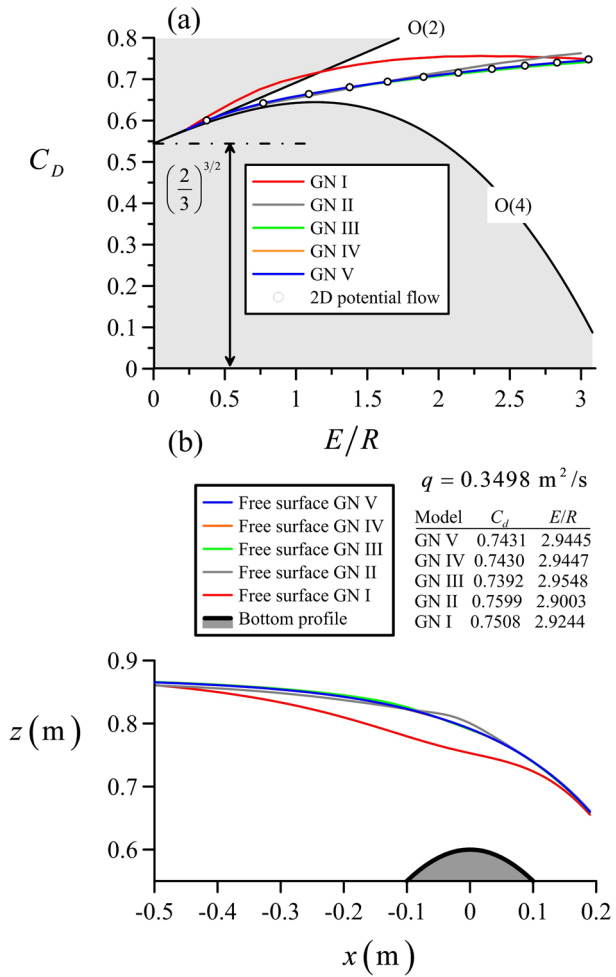
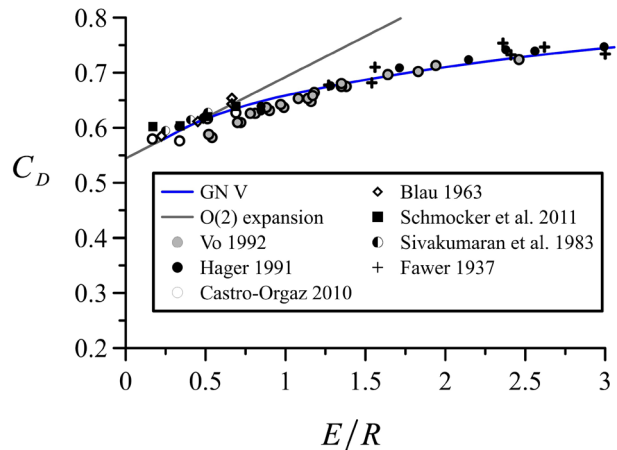


**Fig. 11** Comparison of GN V level theory with experimental data from different sources



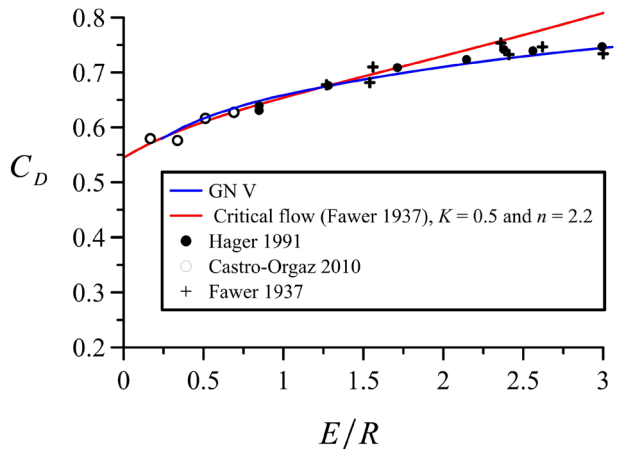
$$\frac{1}{R} = \frac{1}{R_b} + \left( \frac{1}{R_b + nh} - \frac{1}{R_b} \right) \sigma^K. \tag{47}$$

where  $K$  and  $n$  are empirical coefficients of the theory, determined by Fawer [31] by fitting his theory to 2D flow net results. Average values  $K=0.5$  and  $n=2.2$  are in general appropriate [11]. Inserting Eq. (47) into an analytical solution of the crest velocity distribution derived from the Euler equations, the result is used to compute the discharge  $q$  for a given head  $E$ , which is also a function of the undetermined crest flow depth. The unit discharge is then maximised (equivalent to setting critical flow conditions) with respect to the crest flow depth, producing as an outcome  $C_D$  for this value of  $E$ . The predicted  $C_D$  by Fawer’s [31] critical flow theory is compared in Fig. 12 to GN V theory and experiments. Both theories are close to each other up to  $E/R=1.5$ , diverging onwards. It means that, for Fawer theory, a different data pair  $(K, n)$  should be used to fit the GN V results at larger heads. The present comparison is a new validation of Fawer theory, which is demonstrated to be again a good modeling option for the discharge characteristics, when adequate  $(K, n)$  values are used.

### 4.3 Limitations linked to bed geometry: discontinuities and bed steepness

The development of GN theory assumes that the variables  $h, z_b$  and  $\mathbf{u}$  are continuous and differentiable at least to third order [75]. The new experiments conducted in this work with a log-normal bed profile (Fig. 8) were specifically designed to verify this starting assumption and check the accuracy of GN V theory. However, this assumption may be drastic for handling a real uneven bathymetry, where there may not be continuity in the bed high order derivatives. Therefore, Demirbilek and Webster [27] included in their GNWAVE model a post-processing of the actual bed bathymetry where a numerical filter was used to its smoothing. This ensures up to certain limits that  $dz_b/dx, d^2z_b/dx^2$  and  $d^3z_b/dx^3$  can be determined with enough accuracy. Additionally, Webster and Wehausen [88] found that the GNWAVE model failed to produce solutions where the bed steepness was more than approximately  $40^\circ$ . Given that, in GN theory, no scales are used, and no terms are throw out, the only way to test the limitations of the theory for handling topography is to produce a solution and compare it with relevant data [88]. Therefore, the purpose of this section is

**Fig. 12** Comparison of Fawer’s [31] critical flow theory with level V Green-Naghdi theory and experiments

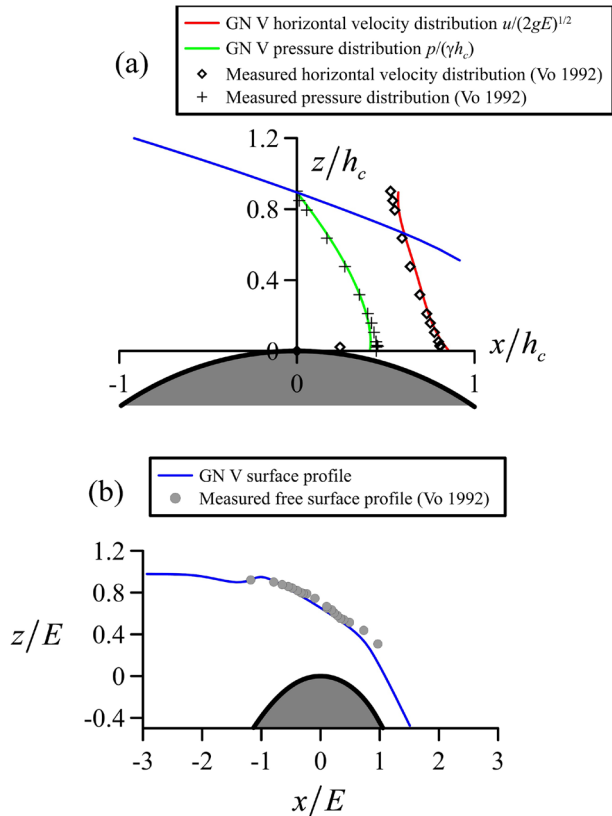


to examine the limitations of the GN theory for handling discontinuities and steep slopes in sill overflows.

We have considered a test by Vo [84] on a circular-crested weir of radius 0.1516 m elevated 1 m from the flume bed. Upstream and downstream ramps of 60° and 45°, respectively, were used [84], test No. 420). The measured velocity and pressure distributions at the crest, and the flow profile, are plotted in Fig. 13a and b. This set up is continuous in  $z_b$ , discontinuous in  $dz_b/dx$  at the intersections of the ramps with the horizontal floor of the flume, and discontinuous in  $d^2z_b/dx^2$  and  $d^3z_b/dx^3$  at the points of tangency of the ramps with the circular arch. Therefore, this is a challenging bed profile for simulations with GN theory.

A first run of GN theory without doing any treatment of the bed indicated that, at the downstream side of the weir, where the flow is supercritical, none of the discontinuities had an effect. However, upstream of the crest, at both the joining point of the flume and the upstream ramp, and at the tangency point of the upstream ramp with the cylinder, distortions of the flow profile were observed. The upstream effect was easily removed using a 5th-order polynomial as transition curve, given that the behavior is similar to Boussinesq equations, which also require this type of bed post-processing [15]. A simulation of GN V theory after this modification is presented in Fig. 13. Observe the dip in the free surface near the beginning of the circular arch (Fig. 13b). No attempts were made to remove this effect, to check if it had an impact of the crest flow conditions.

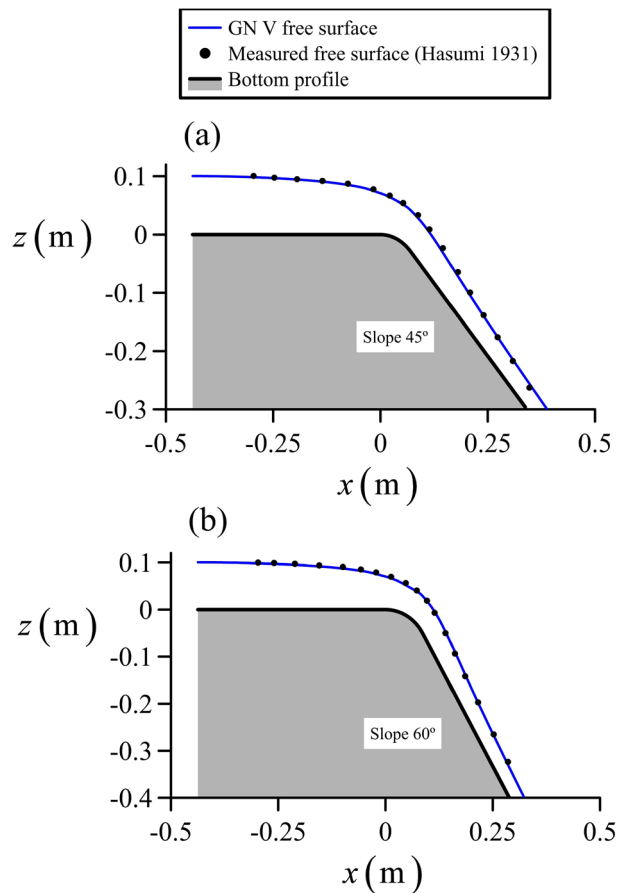
**Fig. 13** Flow over circular-crested weir. Comparison of GN V theory with experiments [84] **a** crest velocity and pressure distributions, **b** free surface profile,  $q=0.08 \text{ m}^2/\text{s}$ . Here  $E$  is the crest specific energy and  $h_c=(q^2/g)^{1/3}$  the critical depth



Predicted GN V crest velocity and pressure distributions are presented in Fig. 13a and compared with the experimental data [84], resulting in a fair agreement. The predicted flow profile is also in reasonable agreement with experiments in the crest zone. The conclusion of this test is that discontinuities in  $z_b$ ,  $dz_b/dx$ ,  $d^2z_b/dx^2$  and  $d^3z_b/dx^3$  in fact have an adverse effect on modeling, and transition curves, like those used in Boussineq models, are needed to remove them when applying GN theory. However, without removing completely the discontinuities, predictions of the GN theory are rather good in the critical section of the overflow, which is the crest.

It is obvious that a bottom slope with  $90^\circ$  of inclination will need resort to the so-called jump conditions for assembling portions of the flow profile up-and downstream from a vertical bed. For a very slight bottom inclination one would expect that all the derivatives  $dz_b/dx$ ,  $d^2z_b/dx^2$  and  $d^3z_b/dx^3$  be small. However, it is unknown up to which steepness before  $90^\circ$  the GN theory can be applied. Webster and Wehausen [88] found solution failure for a bed steepness more than  $40^\circ$ . Therefore, a closer examination of the issue was accomplished here using the transition from mild to steep slopes [44]. Although this is not properly a sill overflow test, it models the effects of bottom slopes on the flow past a control section, which is also basically a fundamental characteristic of the overflow problem. In the slope transition problem (Fig. 14), an approaching

**Fig. 14** Comparison of GN V theory and experiments [44] for flow at steep slopes of **a**  $45^\circ$ , **b**  $60^\circ$ ,  $q=0.1 \text{ m}^2/\text{s}$



critical flow accelerates over a horizontal flume towards a transitional curve designed with a circular arc of radius 0.1 m, which is made tangent to downstream ramps of  $45^\circ$  and  $60^\circ$ . The data of Hasumi [44] for the flow profiles in these transitions is plotted in Fig. 14. Simulations of GN V theory presented in the same figure show a good agreement with experiments, demonstrating that, for the kind of problems examined herein, the GN theory has validity up to a rather high steepness. For  $90^\circ$ , the theory cannot be applied unless jump conditions are developed.

## 5 Discussion of results and limitations

In this work, variational GN models up to level V were developed by expanding the horizontal velocity using as base functions the shifted Legendre polynomials, and determining the vertical velocity and fluid pressure by integration of the continuity and  $z$ -momentum equations, respectively. Although the base functions and closure for  $w$  and  $p$  are different from those used previously by Shields and Webster [75] and Webster et al. [91], the structure of the equations is the same. It does not have implications on the accuracy of either method, but suggests that the differential equations of the theory generally obey a determined mathematical structure, which makes the efficient numerical method by Demirbilek and Webster [26, 27] of general applicability.

A key feature of the theory is that kinematic boundary conditions are exactly satisfied as well as conservation of mass and  $z$ -momentum. In contrast,  $x$ -momentum is satisfied in a weighted residual sense only. Increasing the level of the theory (namely increasing the number of terms in the  $u$ -expansion), the solution converged for the sill problem, implying that the  $x$ -momentum balance was satisfied with greater accuracy. In contrast, perturbation expansions are only asymptotic thus limited to low  $E/R$ .

By comparing the simulations of the five levels of the theory considered, it was found that a very significant improvement occurs when using the GN II theory instead of the GN I. Although progressive improvements were found when jumping from one level of the theory to the next onwards, until convergence, these were in general moderate to small adjustments of the already robust GN II theory. Therefore, the GN II theory is the minimum advised in practice.

An improved  $x$ - $\psi$  method to construct a vertically resolved fully non-linear potential flow solution for large sill overflows was developed with an implicit treatment of the free surface iteration. Solution failure of previous schemes when iterating the discrete free-surface Bernoulli equation was examined and practical advice given to obtain converged solutions. The sensitivity of solutions upstream of the sill crest was elucidated, showing that changes in the free surface are maximal when the Bernoulli constant varies by a small quantity, suggesting the need of a careful iteration method and good initial solution.

The GN V theory is adopted as the practical model for sill overflows, given the excellent approximation to the problem. The free surface streamline generated by GN V theory has an additional important utility, namely its use as initial free surface in the 2D irrotational flow solver. The construction of such solutions needs a good initial surface for convergence of the free-surface discrete Bernoulli equation iterations.

A limitation inherent to the GN theory is that the bed bathymetry  $z_b(x)$  shall be continuous and differentiable. This poses a problem at discontinuities like a bottom step. In these cases, generalized jump conditions need to be formulated for the high-level equations, thereby assembling solutions at each side of the bed discontinuity. In the present work, we generally considered continuous bed profiles, and the limitation was not present. The same limitation is shared by other theories, like Boussinesq equations. New experiments conducted in a large-scale obstacle constructed with a log-normal shape demonstrated the accuracy of GN theory for handling flows over a rapidly changing bed shape.

Another limitation found by Shields [74], Shields and Webster [75] and Demirbilek and Webster [26, 27] is that the GN high-level theory cannot be applied for breaking waves. When a wave is about to break, singular matrices were produced in the block Thomas algorithm, leading to solution failure. This was verified during this research. It means that, in principle, the GN theory cannot be applied to hydraulic jump and bores, like those that may appear at the lee side of a sill. However, the solution failure is unclear and may be linked to the numerical method used by Demirbilek and Webster [26, 27], the one also used here, which seems to be adequate to simulate continuous flows only, but not for discontinuous solutions. The main physical assumption of GN theory is that the horizontal velocity admits an expansion which basically results in high-order polynomials depending on elevation  $z$ . This is in general a good choice for open channel flows, even for bores and hydraulic jumps, due to the ability of a high order polynomial to mimic recirculation zones, like a roller. Therefore, there seems to be no physical reason to discard use of high-level GN theory for breaking waves, but a more robust numerical method to deal with shocks seems advisable. The robust finite-volume solver developed by Cantero-Chinchilla et al. [8] for a theory, which is similar to GN II, simulated breaking waves and jumps, reinforcing the above arguments. Further research is needed to clarify these aspects of the GN theory. In the present work the actual limitation discussed had no impact, given the smooth solutions across the sill crest without hydraulic jumps at the lee side.

The high-level Green–Naghdi (GN level V or GN V) theoretical development, the earlier Serre–Green–Naghdi (SGN) theory (i.e. the lowest level GN I) and the irrotational flow theory of ideal fluid were applied for steady overflow conditions up to  $E/R=3$ . Therefore, a limitation of the application developed in the current research is its validity for steady flow conditions up to this overflow limit. Recent laboratory experimentation using half-round circular weirs considered unsteady overflows with larger ratios, resulting in several major technical challenges. Recently, a test case study of round-crested un-ventilated weirs reported several discrepancies among 20 data sets obtained at 20 different hydraulic facilities worldwide for the same boundary condition specifications [81]. A number of subsequent studies with half-round circular crested weir pointed to the occurrence of non-linear instabilities, including hysteresis [20] and cyclic behaviour [21]. Chanson and Memory [21] concluded to the existence of complicated physical modelling characterised by transient flow patterns spanning over relatively long durations [21]. Such instabilities above half-round circular weirs result in a large scatter in  $C_D$  for  $E/R > 3$ , with marked differences between data sets obtained with increasing discharge  $q$  versus decreasing discharge. The time variation of the water depth above the sill crest showed the superposition of slow fluctuations and very rapid fluctuations in these experiments. The former was associated with changes in flow patterns between attached and detached nappes, observed in a very slow

quasi-cyclic manner, yielding large changes in upstream water depth, depth above the sill crest and discharge coefficient. The cyclic flow patterns did not develop into steady flow condition, despite experiments conducted for very long durations, i.e. over three hours. The existence of non-linear instabilities and cyclic flow patterns linked to unsteady flow conditions constitute a limitation of the current application, which shall be explored in future research of GN theory for application to channel structures.

## 6 Concluding remarks

The main concluding remarks of this work on the high-level Green-Naghdi (GN) theory are as follows:

It is found that GN I theory does not yield an accurate modeling approach for the flow profile, discharge coefficient and crest velocity and pressure distributions for  $E/R > 0.7$ . The GN II level theory is in general a good choice for relatively large heads, i.e., up to  $E/R = 1.75$ , with a small increase in computational load over the GN I theory.

The Green–Naghdi expansions are found to be convergent for the sill-controlled flow problem, in contrast to the shallow water expansions, which are asymptotic only. GN V theory is adopted as the practical model, given that it resulted in excellent agreement with the 2D irrotational flow results and experiments available in the literature and newly conducted ones, producing good  $C_D$  predictions for relatively large overflows, e.g. up to  $E/R = 3$ .

The GN V theory was compared with approximate critical flow computations with curved streamlines due to Fawer [31], resulting in a good agreement for average calibrated parameters of the latter approximate theory. The slope limitation of GN V theory for sill overflows is in principle  $60^\circ$  given the excellent behavior of the theory when compared with experiments.

The GN V theory was not tested for unsteady sill overflow conditions, such as the occurrence of non-linear instabilities and cyclic flow behaviors observed on half-round circular-crested weirs for high upstream head above crest, constituting a path of future application of GN theory to prototype and laboratory structures.

## Appendix A: Matrix formulation for GN II equations

In this section we provide the symbolic output for the modeling approach GN II. Green–Naghdi theory of level II starts assuming that  $u = u_0 + u_1\phi_1$ . The expansions for  $(u, w, p)$  are as follows:

$$\begin{aligned}
 u &= u_0 - (2\sigma - 1)u_1; \\
 w &= z_{bx}u_0 + z_{bx}u_1 - \sigma u_0x^h - \sigma u_1x^h - 2\sigma z_{bx}u_1 + \sigma^2 u_1x^h - \sigma^2 hxu_1; \\
 p/(\rho h g) &= (u_0x^h + hxu_0)^2/g - \sigma h + h - (u_0tx^h)^2/(2g) - (ultx^h)^2/(6g) - (u_0x^2h)^2/(2g) + (hx^2u_0^2)/g + (hx^2u_1^2)/(6g) + (\sigma^2 u_0tx^h)^2/(2g) + (\sigma^2 ultx^h)^2/(2g) - (\sigma^3 ultx^h)^2/(3g) - (hxult^h)/(3g) + (u_0tz_{bx}h)/g - (\sigma^2 u_0x^2h^2)/(2g) - (\sigma^2 u_1x^2h^2)/(2g) + (\sigma^3 u_1x^2h^2)/g - (\sigma^4 u_1x^2h^2)/(2g) - (2\sigma^3 u_1x^2h^2)/(3g) + (\sigma^4 u_1x^2h^2)/(2g) + (u_1x^h(u_0x^h + hxu_0))/(3g) - (2hxu_0(u_0x^h + hxu_0))/g + (4hxu_1(u_0x^h + hxu_0))/(3g) + (hxx^h u_1^2)/(6g) - (u_0xx^h^2 u_0)/(2g) + (u_0xx^h^2 u_1)/(6g) - (u_1xx^h^2 u_0)/(6g) - (4hx^2 u_0 u_1)/(3g) - (2z_{bx}u_0(u_0x^h + hxu_0))/g + (z_{bx}u_1(u_0x^h + hxu_0))/g + (z_{bx}h^2 u_0^2)/g + (z_{bx}h^2 u_1^2)/(3g) + (h^2 u_1(u_0xx^h + hxxu_0 + 2hxu_0x))/g + (2hxz_{bx}u_0^2)/g + (hxz_{bx}u_1^2)/(3g) - (\sigma z_{bxx}h^2 u_0^2)/g - (\sigma z_{bxx}h^2 u_1^2)/g + (\sigma^3 hxult^h)/(3g) + (\sigma^2 ultz_{bx}h)/g - (\sigma^3 u_1x^h(u_0x^h + hxu_0))/(3g) + (2\sigma^3 hxu_1(u_0x^h + hxu_0))/(3g) + (\sigma^3 hxx^h u_1^2)/(3g) - (\sigma^4 hxx^h u_1^2)/(2g) + (\sigma^2 u_0xx^h^2 u_0)/(2g) + (\sigma^2 u_0xx^h^2 u_1)/(2g) + (\sigma^2 u_1lxx^h^2 u_1)/(2g) - (2\sigma^3 u_0xx^h^2 u_1)/(3g) - (\sigma^3 u_1lxx^h^2 u_0)/(3g) - (\sigma^3 u_1lxx^h^2 u_1)/g + (\sigma^4 u_1lxx^h^2 u_1)/(2g) - (2\sigma^3 hx^2 u_0 u_1)/(3g) + (\sigma^2 z_{bx}u_1(u_0x^h + hxu_0))/g + (2\sigma^2 z_{bxx}h^2 u_1^2)/g - (4\sigma^3 z_{bxx}h^2 u_1^2)/(3g) - (\sigma^2 u_0x^h u_1x^h^2)/g + (\sigma^3 u_0x^h u_1x^h^2)/g - (\sigma^3 h^2 u_1(u_0xx^h + hxxu_0 + 2hxu_0x))/g - (\sigma^2 hxz_{bx}u_1^2)/g + (2\sigma^3 hxz_{bx}u_1^2)/(3g) - (hxx^h u_0 u_1)/(3g) - (hxu_0x^h u_1)/g - (2hxu_1x^h u_0)/(3g) + (hxu_1x^h u_1)/(3g) + (3u_0x^h z_{bx}u_0)/g - (u_0x^h z_{bx}u_1)/g + (2u_1x^h z_{bx}u_1)/g - (hxz_{bx}u_0 u_1)/g - (\sigma u_0tz_{bx}h)/g - (\sigma ultz_{bx}h)/g - (2\sigma z_{bxx}h^2 u_0 u_1)/g - (\sigma u_0x^h z_{bx}u_0)/g - (\sigma u_0x^h z_{bx}u_1)/g - (\sigma u_1x^h z_{bx}u_0)/g + (\sigma^3 hxx^h u_0 u_1)/(3g) + (2\sigma^2 z_{bxx}h^2 u_0 u_1)/g - (\sigma^3 hxu_0x^h u_1)/g + (2\sigma^3 hxu_1x^h u_0)/(3g) - (\sigma^3 hxu_1x^h u_1)/(3g) + (\sigma^2 u_1x^h z_{bx}u_0)/g + (\sigma^2 u_1x^h z_{bx}u_1)/g - (2\sigma^3 u_1x^h z_{bx}u_1)/(3g) - (\sigma^2 hxz_{bx}u_0 u_1)/g;
 \end{aligned}$$

Note  $u$  is a polynomial of degree 1 in  $\sigma$ ,  $w$  is a polynomial of degree 2 in  $\sigma$  and  $p$  is a polynomial of degree 4 in  $\sigma$ . Using these expansions for  $(u, w, p)$ , the Green–Naghdi evolution equations found are:

$$\begin{pmatrix} A_{11} & A_{12} \\ A_{21} & A_{22} \end{pmatrix} \mathbf{f} + \begin{pmatrix} B_{11} & B_{12} \\ B_{21} & B_{22} \end{pmatrix} \frac{\partial \mathbf{f}}{\partial x} + \begin{pmatrix} C_{11} & C_{12} \\ C_{21} & C_{22} \end{pmatrix} \frac{\partial^2 \mathbf{f}}{\partial x^2} = \begin{pmatrix} g_1 \\ g_2 \end{pmatrix}$$

$$\mathbf{f} = \frac{\partial \mathbf{u}}{\partial t}, \quad \mathbf{u} = \begin{pmatrix} u_0 \\ u_1 \end{pmatrix}, \quad (48)$$

where the coefficients are stated below:

**Equation 1 ( $j = 1$ )**

$$\begin{aligned} g_1 = & g * z b x * h + g * h x * h + u_0 x * h * u_0 + (h x * u_1^2) / 3 + (h x^3 * u_1^2) / 10 \\ & + (3 * h x x x * h^2 * u_1^2) / 20 + (z b x x x * h^2 * u_0^2) / 2 + \\ & (z b x x x * h^2 * u_1^2) / 6 + h x * u_0 x^2 * h^2 + (h x * u_1 x^2 * h^2) / 5 + \\ & u_0 x^2 * z b x * h^2 + (u_1 x^2 * z b x * h^2) / 3 + (h x * z b x^2 * u_1^2) / 3 + \\ & (h x^2 * z b x * u_1^2) / 3 + (2 * u_1 x * h * u_1) / 3 - (u_0 x x x * h^3 * u_0) / 3 + \\ & (5 * u_0 x x x * h^3 * u_1) / 12 - (u_1 x x x * h^3 * u_0) / 12 + (u_1 x x x * h^3 * u_1) / 60 \\ & + (u_0 x * u_0 x x * h^3) / 3 + (u_0 x * u_1 x x * h^3) / 12 + \\ & (7 * u_1 x * u_0 x x * h^3) / 12 - (u_1 x * u_1 x x * h^3) / 60 + (h x * h x x * h * u_1^2) / 2 \\ & - (z b x x x * h^2 * u_0 * u_1) / 3 + (3 * h x^2 * u_0 x * h * u_1) / 2 - \\ & (h x^2 * u_1 x * h * u_0) / 2 + (7 * h x^2 * u_1 x * h * u_1) / 10 - h x * u_0 x x * h^2 * u_0 + \\ & 2 * h x * u_0 x x * h^2 * u_1 - (h x * u_1 x x * h^2 * u_0) / 2 + \\ & (3 * h x * u_1 x x * h^2 * u_1) / 10 + (3 * h x x * u_0 x * h^2 * u_1) / 4 - \\ & (h x x * u_1 x * h^2 * u_0) / 4 + (11 * h x x * u_1 x * h^2 * u_1) / 20 + \\ & h x * z b x x * h * u_0^2 + (h x * z b x x * h * u_1^2) / 2 + (h x x * z b x * h * u_1^2) / 3 + \\ & u_0 x * z b x^2 * h * u_0 + (2 * u_1 x * z b x^2 * h * u_1) / 3 + \\ & (3 * u_0 x * z b x x * h^2 * u_0) / 2 - (u_0 x * z b x x * h^2 * u_1) / 2 - \\ & (u_1 x * z b x x * h^2 * u_0) / 2 + (u_0 x x * z b x * h^2 * u_1) / 3 - \\ & (u_1 x x * z b x * h^2 * u_0) / 3 + (2 * u_1 x * z b x x * h^2 * u_1) / 3 + \\ & (u_1 x x * z b x * h^2 * u_1) / 3 + h x * u_0 x * u_1 x * h^2 + z b x * z b x x * h * u_0^2 + \\ & (z b x * z b x x * h * u_1^2) / 3 - (2 * h x * z b x x * h * u_0 * u_1) / 3 + \\ & h x * u_0 x * z b x * h * u_0 + (2 * h x * u_0 x * z b x * h * u_1) / 3 - \\ & (2 * h x * u_1 x * z b x * h * u_0) / 3 + (4 * h x * u_1 x * z b x * h * u_1) / 3; \end{aligned}$$

**Equation 2 (j = 2)**

$$\begin{aligned}
g_2 = & (h_{xxx} \cdot h^2 \cdot u_1^2) / 60 - (h_x^3 \cdot u_1^2) / 30 + \\
& (z_{bxxx} \cdot h^2 \cdot u_0^2) / 6 + (z_{bxxx} \cdot h^2 \cdot u_1^2) / 30 + \\
& (h_x \cdot u_{1x}^2 \cdot h^2) / 15 + (2 \cdot u_{1x}^2 \cdot z_{bx} \cdot h^2) / 15 - \\
& (h_x^2 \cdot z_{bx} \cdot u_1^2) / 15 + (u_{0x} \cdot h \cdot u_1) / 3 + (u_{1x} \cdot h \cdot u_0) / 3 - \\
& (u_{0xxx} \cdot h^3 \cdot u_0) / 12 + (u_{0xxx} \cdot h^3 \cdot u_1) / 15 - (u_{1xxx} \cdot h^3 \cdot u_0) / 30 + \\
& (u_{0x} \cdot u_{0xx} \cdot h^3) / 12 + (u_{0x} \cdot u_{1xx} \cdot h^3) / 30 + (2 \cdot u_{1x} \cdot u_{0xx} \cdot h^3) / 15 \\
& - (h_x \cdot h_{xx} \cdot h \cdot u_1^2) / 30 - (3 \cdot h_x^2 \cdot u_{0x} \cdot h \cdot u_1) / 10 + \\
& (h_x^2 \cdot u_{1x} \cdot h \cdot u_0) / 10 - (h_x^2 \cdot u_{1x} \cdot h \cdot u_1) / 30 - \\
& (h_x \cdot u_{1xx} \cdot h^2 \cdot u_0) / 10 + (h_x \cdot u_{1xx} \cdot h^2 \cdot u_1) / 30 + \\
& (3 \cdot h_{xx} \cdot u_{0x} \cdot h^2 \cdot u_1) / 20 - (h_{xx} \cdot u_{1x} \cdot h^2 \cdot u_0) / 20 + \\
& (h_{xx} \cdot u_{1x} \cdot h^2 \cdot u_1) / 12 - (h_{xx} \cdot z_{bx} \cdot h \cdot u_1^2) / 15 + \\
& (u_{0x} \cdot z_{bx}^2 \cdot h \cdot u_1) / 3 + (u_{1x} \cdot z_{bx}^2 \cdot h \cdot u_0) / 3 + \\
& (u_{0x} \cdot z_{bxx} \cdot h^2 \cdot u_0) / 2 + (u_{0xx} \cdot z_{bx} \cdot h^2 \cdot u_0) / 3 - \\
& (u_{0xx} \cdot z_{bx} \cdot h^2 \cdot u_1) / 3 + (u_{1x} \cdot z_{bxx} \cdot h^2 \cdot u_1) / 6 + \\
& (u_{1xx} \cdot z_{bx} \cdot h^2 \cdot u_1) / 15 + (h_x \cdot u_{0x} \cdot u_{1x} \cdot h^2) / 5 + \\
& (h_x \cdot z_{bxx} \cdot h \cdot u_0 \cdot u_1) / 3 + (2 \cdot z_{bx} \cdot z_{bxx} \cdot h \cdot u_0 \cdot u_1) / 3 - \\
& (h_x \cdot u_{0x} \cdot z_{bx} \cdot h \cdot u_1) / 3 + (h_x \cdot u_{1x} \cdot z_{bx} \cdot h \cdot u_0) / 3 - \\
& (h_x \cdot u_{1x} \cdot z_{bx} \cdot h \cdot u_1) / 15;
\end{aligned}$$

**Equation 1 (j = 1)**

$$\begin{aligned}
A_{11} = & h + z_{bx}^2 \cdot h + (z_{bxx} \cdot h^2) / 2 + h_x \cdot z_{bx} \cdot h; \\
A_{12} = & - (h_x^2 \cdot h) / 2 - (h_{xx} \cdot h^2) / 4 - (z_{bxx} \cdot h^2) / 6 - \\
& (2 \cdot h_x \cdot z_{bx} \cdot h) / 3;
\end{aligned}$$

$$B_{11} = -h_x \cdot h^2;$$

$$B_{12} = - (h_x \cdot h^2) / 2 - (z_{bx} \cdot h^2) / 3;$$

$$C_{11} = -h^3 / 3;$$

$$C_{12} = -h^3 / 12;$$

**Equation 2 (j = 2)**

$$\begin{aligned}
 A_{21} &= (z_{bxx} * h^2) / 6; \\
 A_{22} &= (h * h_x^2) / 10 + (h * h_x * z_{bx}) / 3 + (h * z_{bx}^2) / 3 + h / 3 - \\
 &\quad (h_{xx} * h^2) / 20; \\
 B_{21} &= (z_{bx} * h^2) / 3; \\
 B_{22} &= - (h_x * h^2) / 10; \\
 C_{21} &= -h^3 / 12; \\
 C_{22} &= -h^3 / 30;
 \end{aligned}$$

**Appendix B: Discrete free-surface Bernoulli equation**

The determination of the free surface position with the discrete Bernoulli equation is a complex non-linear problem. To our knowledge, the difficulties are commented in some works [22, 56, 79], but these are not explored neither explained. Here, we provide an outlook to the problem and some practical advice.

The discrete free surface Bernoulli equation at a position  $i$  of the mesh is using the  $x$ - $\psi$  mapping

$$H(i) = z(i, M) + \frac{1}{2g} \left[ \frac{2\Delta\psi}{3z(i, M) - 4z(i, M - 1) + z(i, M - 2)} \right]^2 \left[ 1 + \left( \frac{z(i + 1, M) - z(i - 1, M)}{2\Delta x} \right)^2 \right] \quad (49)$$

For a given value of  $H(i)$ , this is a cubic equation with three possible roots for  $z(i, M)$ , the coordinate of the free surface at that node. It was found that the three possible roots  $z(i, M)$  for a given  $H(i)$  value are real, and of a magnitude very similar. This makes exceedingly difficult to determine with a root finding algorithm like the Newton–Raphson method which one is the physically correct root. Further analysis was undertaken here to get a better understanding.

We have considered the flow over the Gaussian hump test in Fig. 7. Using the final converged two-dimensional solution, the function  $H(i)$  is plotted versus  $z(i, M)$  in Fig. 15 at the crest section ( $x = 0$  m) and upstream of the sill crest ( $x = -0.5$  m), in the zone of uncertainty according to Cheng et al. [22]. At both sections, the actual flow solution is plotted. We have also determined the three roots for the target energy head, which are for  $x = 0$  m:

$$(S1, S2, S3) = (0.349512991389396, 0.302113856953000, 0.294138840891281).$$

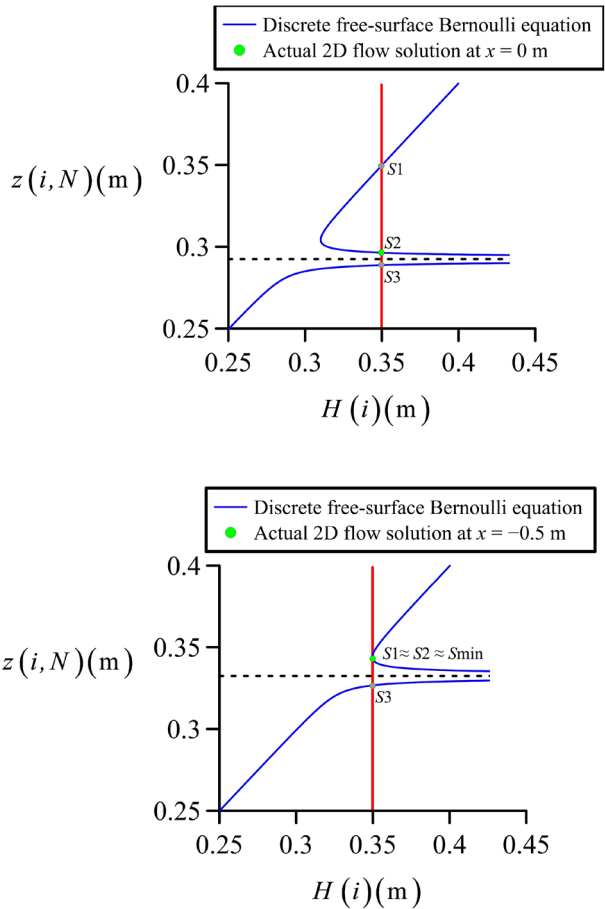
For the section at  $x = -0.5$  m the three roots are:

$$(S1, S2, S3) = (0.344987598039410, 0.343003371274220, 0.326689053566463).$$

The roots are also marked in Fig. 15.

At the sill crest two of the roots are found to be remarkably close to each other (S2 and S3), one of them being unphysical and corresponding to  $u_s < 0$  (solution S3). The condition of zero surface velocity ( $u_s = 0$ ) is given analytically by  $z(i, M) = -[-4z(i, M - 1) + z(i, M - 2)]/3$ , which is plotted as a dotted line in Fig. 15. It is in general not possible to decide with the Newton–Raphson iteration scheme which of the roots is the physically correct one, given that all are real and very close to each other at the weir

**Fig. 15** Discrete free surface Bernoulli equation diagram at two sections for the gaussian flow test of Fig. 7 indicating the actual 2D flow solution and the three possible roots



crest. Upstream of the crest the situation is even more complex, given that the two roots with  $u_s > 0$  (S1 and S2) are almost identical from a numerical standpoint and close to the point of minimum  $H(i)$ . Therefore, a small variation in  $H(i)$  during the iteration of the surface node there will produce a very large variation in  $z(i, M)$  given that the changes  $dz(i, M)/dH(i)$  are maximal in this zone of the curve. Note that the curves presented in Fig. 15 are a representation of the discrete free surface Bernoulli equation and are unrelated to the minimum specific diagram of hydrostatic flows. A minimum in  $H(i)$  is unrelated to critical flow.

The above considerations suggest the necessity of using a good initial solution for all the free surface nodes in the 2D model, e.g., that given by GN V, and during the iterations, a damping factor of the order of 0.1 is to be applied to the correction vector  $\Delta z_s$ , ensuring that the physically correct root is approached in the zone of uncertainty upstream of the sill crest. The corrections are not allowed to drop below  $z(i, M) = -[-4z(i, M - 1) + z(i, M - 2)]/3$ , which is therefore a lower bound.

**Author contributions** All the authors equally contributed to all the stages of this research.

**Funding** The work of O. Castro-Orgaz was supported by the Spanish project PID2020-114688RB-I00 funded by MCIN/AEI/<https://doi.org/10.13039/501100011033/> FEDER “Una manera de hacer Europa” and grant María de Maeztu for Centers and Units of Excellence in R&D (Ref. CEX2019-000968-M). The work of T. Morales de Luna was supported by the Spanish project PID2020-114688RB-I00. F. Cantero-Chinchilla was funded by MCIN/AEI/[https://doi.org/10.13039/501100011033](https://doi.org/10.13039/501100011033/) and the NextGeneration EU/PRTR through Juan de la Cierva program (IJC2020-042646-I).

## Declarations

**Conflict of interest** The authors declare that they have no conflict of interest.

## References

- Abramowitz M, Stegun IA (1972) Handbook of mathematical functions with formulas, graphs, and mathematical tables, 10th edn. Wiley, New York
- Bertin X, Mendes D, Martins K, Fortunato AB, Lavaud L (2019) The closure of a shallow tidal inlet promoted by infragravity waves. *Geophys Res Lett* 46(12):6804–6810
- Blau E (1963) Der Abfluss und die hydraulische Energieverteilung über einer parabelförmigem Wehrschwelle (Flow and the hydraulic energy distribution over a parabolic weir). *Mitteilung 7*, 5–72. Forschungsanstalt für Schiffahrt, Wasser und Grundbau, Berlin [in German]
- Boadway JD (1976) Transformation of elliptic partial differential equations for solving two dimensional boundary value problems in fluid flow. *Int J Num Meth Engng* 10(3):527–533
- Bush AW (1992) Perturbation methods for engineers and scientists. CRC Press, Boca Raton
- Cantero-Chinchilla F, Castro-Orgaz O, Dey S, Ayuso JL (2016) Non-hydrostatic dam break flows. I: physical equations and numerical schemes. *J Hydraul Eng* 142(12):04016068
- Cantero-Chinchilla F, Castro-Orgaz O, Dey S, Ayuso JL (2016) Non-hydrostatic dam break flows. II: one-dimensional depth-averaged modelling for movable bed flows. *J Hydraul Eng* 142(12):04016069
- Cantero-Chinchilla FN, Castro-Orgaz O, Khan AA (2018) Depth-integrated nonhydrostatic free-surface flow modelling using weighted-averaged equations. *Int J Numer Meth Fluids* 87(1):27–50
- Cantero-Chinchilla FN, Castro-Orgaz O, Khan AA (2019) Vertically-averaged and moment equations for flow and sediment transport. *Adv Water Resour* 132:103387
- Cantero-Chinchilla FN, Bergillos RJ, Castro-Orgaz O (2020) Nearshore coastal flow processes using weighted-averaged equations. *Ocean Eng* 211:107480
- Castro-Orgaz O (2010) Steady open channel flows with curved streamlines: the Fawer approach revised. *Environ Fluid Mech* 10(3):297–310
- Castro-Orgaz O (2010) Approximate modeling of 2D curvilinear open channel flows. *J Hydraul Res* 48(2):213–224
- Castro-Orgaz O, Hutter K, Giraldez JV, Hager WH (2015) Non-hydrostatic granular flow over 3D terrain: new Boussinesq-type gravity waves? *J Geophys Res-Earth Surf* 120(1):1–28. <https://doi.org/10.1002/2014JF003279>
- Castro-Orgaz O, Chanson H (2016) Minimum specific energy and transcritical flow in unsteady open channel flow. *J Irrig Drain Eng* 142(1):04015030
- Castro-Orgaz O, Hager WH, Cantero-Chinchilla FN (2022) Shallow flows over curved beds: application of the Serre–Green–Naghdi theory to weir flow. *J Hydraul Eng* 148(1):04021053
- Castro-Orgaz O, Cantero-Chinchilla FN, Hager WH (2022) High-order shallow water expansions in free surface flows: application to steady overflow processes. *Ocean Eng* 250:110717
- Castro-Orgaz O, Cantero-Chinchilla FN, Chanson H (2022) Shallow fluid flow over an obstacle: higher-order non-hydrostatic modeling and breaking waves. *Environ Fluid Mech* 22(4):971–1003
- Castro-Orgaz O, Hager WH, Katopodes ND (2023) Variational models for nonhydrostatic free-surface flow: a unified outlook to maritime and open-channel hydraulics developments. *J Hydraul Eng* 149(7):04023014
- Chanson H (2006) Minimum specific energy and critical flow conditions in open channels. *J Irrigat Drain Engng* 132(5):498–502
- Chanson H (2020) Half-round circular crested weir: on hysteresis, instabilities and head-discharge relationship. *J Irrigat Drainage Eng* 146(6):04020008
- Chanson H, Memory O (2022) Hysteresis, non-linearity and instabilities on circular crested weir. Proceedings of 30th Hydrology and Water Resources Symposium HWRS2022, Brisbane, Australia,

- 30 November–2 December, Published by Engineers Australia, Brisbane, Australia, Paper 156, pp. 1116–1124
22. Cheng AH-D, Liggett JA, Liu PL-F (1981) Boundary calculations of sluice and spillway flows. *J Hydraulics Div ASCE* 107(HY10):1163–1178
  23. Dai S, Sheng J (2022) Numerical investigations of unsteady critical flow conditions over an obstacle using three models. *Phys Fluids* 34:025103
  24. Dao-Yang D, Man-Ling L (1979) Mathematical model of flow over a spillway dam. In: *Proceedings of 13th international congress of large dams New Delhi Q50 (R55)*, pp 959–976
  25. Diersch H-J, Schirmer A, Busch K-F (1977) Analysis of flows with initially unknown discharge. *J Hydr Div ASCE* 103(HY3):213–232
  26. Demirbilek Z, Webster WC (1992a) Application of the Green–Naghdi theory of fluid sheets to shallow-water wave problems: report 1, Model development. US Army Corps. of Eng., Waterways Experiment Station, Rep. No. CERC92–11, Vicksburg, MS
  27. Demirbilek Z, Webster WC (1992b) User's manual and examples for GNWAVE. US Army Corps. of Eng., Waterways Experiment Station, Rep. No. CERC92–11, Vicksburg, MS
  28. Denton RA (1987) Locating and identifying hydraulic controls for layered flow through an obstruction. *J Hydraul Res* 25(3):281–299. <https://doi.org/10.1080/00221688709499271>
  29. Duan WY, Zheng K, Zhao BB, Demirbilek Z, Ertekin RC, Webster WC (2016) On wave-current interaction by the Green–Naghdi equations in shallow water. *Nat Hazards* 84:S567–S583
  30. Farmer DM, Denton RA (1985) Hydraulic control of flow over the sill in Observatory inlet. *J Geophys Res: Oceans* 90(C5):9015–9068. <https://doi.org/10.1029/JC090iC05p09051>
  31. Fawer C (1937) Etude de quelques écoulements permanents à filets courbes (Study of some steady flows with curved streamlines). Thesis. Université de Lausanne, La Concorde, Lausanne, Switzerland (**[in French]**)
  32. Finlayson BA, Scriven LE (1966) The method of weighted residuals—a review. *Applied Mech Rev* 19(9):735–748
  33. Finlayson BA (1972) The method of weighted residuals and variational principles. With applications in fluid mechanics, heat and mass transfer. Academic Press, New York
  34. Gharmry HK, Steffler PM (2002) Two dimensional vertically averaged and moment equations for rapidly varied flows. *J Hydraul Res* 40(5):579–587
  35. Gharmry HK, Steffler PM (2002) Effect of applying different distribution shapes for velocities and pressure on simulation of curved open channels. *J Hydraulic Engng* 128(11):969–982
  36. Gharmry HK, Steffler PM (2005) Two-dimensional depth-averaged modeling of flow in curved open channels. *J Hydraul Res* 43(1):44–55
  37. Green AE, Laws N, Naghdi PM (1974) On the theory of water waves. *Proceed Royal Soci London Series A, Math Phys Sci* 338(1612):43–55
  38. Green AE, Naghdi PM (1976) Directed fluid sheets. *Proc R Soc London, A* 347:447–473
  39. Green AE, Naghdi PM (1976) A derivation of equations for wave propagation in water of variable depth. *J Fluid Mech* 78:237–246
  40. Green AE, Naghdi PM (1984) A direct theory of viscous flow in channels. *Arch Rat Mech Anal* 86(1):39–64
  41. Green AE, Naghdi PM (1986) A nonlinear theory of water waves for finite and infinite depths. *Philos Trans Royal Soc London Ser A* 320:37–70
  42. Green AE, Naghdi PM (1987) Further developments in a nonlinear theory of water waves for finite and infinite depths. *Philos Trans Royal Soc London Ser A* 324:47–72
  43. Guo Y, Wen X, Wu C, Fang D (1998) Numerical modelling of spillway flow with free drop and initially unknown discharge. *J Hydraulic Res* 36(5):785–801
  44. Hasumi M (1931) Untersuchungen über die Verteilung der hydrostatischen Drücke an Wehrkronen und -Rücken von Überfallwehren infolge des abstürzenden Wassers (Studies on the distribution of hydrostatic pressure distributions at overflows due to water flow). *J Dept Agricult Kyushu Imperial Univer* 3(4):1–97
  45. Hager WH (1991) Experiments on standard spillway flow. *Proc ICE* 91(2):399–416
  46. Henderson FM (1966) Open channel flow. MacMillan Co., New York
  47. Ikegawa M, Washizu K (1973) Finite element method applied to analysis of flow over a spillway crest. *Int J Numer Meth Eng* 6:179–189
  48. Kantorovich LV, Krylov VI (1958) Approximate methods of higher analysis. Interscience Publishers Inc., Groningen
  49. Katopodes ND (2019) Free surface flow: computational methods. Butterworth-Heinemann, Oxford
  50. Khan AA, Steffler PM (1996) Vertically averaged and moment equations model for flow over curved beds. *J Hydraulic Engng* 122(1):3–9

51. Khan AA, Steffler PM (1996) Modelling overfalls using vertically averaged and moment equations. *J Hydraulic Engng* 122(7):397–402
52. Levich VG, Krylov VS (1969) Surface-tension driven phenomena. *Ann Rev of Fluid Mech* 1:293–316
53. Liggett JA (1994) *Fluid mechanics*. McGraw-Hill, New York
54. Matthew GD (1963) On the influence of curvature, surface tension and viscosity on flow over round-crested weirs. In: *Proceedings of the institution of civil engineers*, vol 28, pp 557–569
55. Matthew GD (1991) Higher order one-dimensional equations of potential flow in open channels. *Proc ICE* 91(3):187–201
56. Montes JS (1992a) Potential flow analysis of flow over a curved broad crested weir. In: *Proceedings 11th Australasian fluid mechanics conference*. Auckland, pp 1293–1296
57. Montes JS (1992b) A potential flow solution for the free overfall. *Proceeding of ICE* 96(6), 259–266; 112(1), 85–87
58. Montes JS (1994) Potential flow solution to the 2D transition from mild to steep slope. *J Hydraulic Engng* 120(5):601–621
59. Montes JS (1998) *Hydraulics of open channel flow*. ASCE Press, Reston, VA
60. Naghdi PM (1979) Fluid jets and fluid sheets: a direct formulation. In: *Proceeding of 12th Symposium Naval Hydrodynamics*, National Academy of Sciences, Washington D.C, pp 505–515
61. Naghdi PM, Rubin MB (1981) On inviscid flow in a waterfall. *J Fluid Mech* 103:375–387
62. Naghdi PM, Rubin MB (1981) On the transition to planning of a boat. *J Fluid Mech* 103:345–374
63. Naghdi PM, Rubin MB (1982) The effect of curvature at the detachment point of a fluid sheet from a rigid boundary. *Phys Fluids* 25(7):1110–1116
64. Naghdi PM, Vongsarnpigoon L (1986) The downstream flow beyond an obstacle. *J Fluid Mech* 162:223–236
65. Naghdi PM, Vongsarnpigoon L (1986) On steady flow past a sluice gate. *Phys Fluids* 29:3962–3970
66. Naghdi PM, Vongsarnpigoon L (1987) Steady flow past a step. In: *Proceeding of 16th symposium on naval hydrodynamics (Berkeley)*, US. National Academy Press, pp. 151–166
67. Ramamurthy AS, Vo ND (1993) Application of Dressler theory to weir flow. *J Appl Mech* 60(1):163–166
68. Ramamurthy AS, Vo ND (1993) Characteristics of circular-crested weirs. *J Hydraulic Engng* 119(9):1055–1062
69. Ramamurthy AS, Vo ND, Balachandar R (1994) A note on irrotational curvilinear flow past a weir. *J Fluids Engng* 116(2):378–381
70. Rouse H (1932) *The distribution of hydraulic energy in weir flow in relation to spillway design*. MS Thesis. MIT, Boston, MA
71. Rouse H (1938) *Fluid mechanics for hydraulic engineers*. McGraw-Hill, New York
72. Schmockler L, Halldórsdóttir B, Hager WH (2011) Effect of weir face angles on circular-crested weir flow. *J Hydraulic Engng* 137(6):637–643
73. Serre F (1953) Contribution à l'étude des écoulements permanents et variables dans les canaux (Contribution to the study of steady and unsteady channel flows). *La Houille Blanche*, 8(6–7), 374–388; 8(12), 830–887 [in French]
74. Shields JJ (1986) *A direct theory for waves approaching a beach*. Ph.D. Dissertation, University of California at Berkeley
75. Shields JJ, Webster WC (1988) On direct methods in water-wave theory. *J Fluid Mech* 197:171–199
76. Sivakumaran NS, Tingsanchali T, Hosking RJ (1983) Steady shallow flow over curved beds. *J Fluid Mech* 128:469–487
77. Sivakumaran NS (1981) *Shallow flow over curved beds*. PhD thesis. Asian Institute of Technology, Bangkok, Thailand
78. Steffler PM, Jin YC (1993) Depth-averaged and moment equations for moderately shallow free surface flow. *J Hydraulic Res* 31(1):5–17
79. Strelkoff TS (1969) *The solitary wave as a steady flow*. Computer studies of finite-amplitude waves, report n.104, Dept. of Civil Engineering, Stanford University
80. Su CH, Gardner CS (1969) KdV equation and generalizations. Part III: Derivation of Korteweg-de Vries equation and Burgers equation. *J Math Phys* 10(3):536–539
81. Tullis BP, Crookston BM, Bung DB (2019). Weir head-discharge relationships: A multilab exercise. In: *Proceedings of 38th IAHR World Congress, Panama City, 1–6 Sept.*, IAHR Publication, Lucas Calvo Editor, pp. 486–500 (Doi <https://doi.org/10.3850/38WC092019-0806>)
82. Vallentine HR (1969) *Applied hydrodynamics*. Butterworths, London
83. Van Dyke M (1975) *Perturbation methods in fluid mechanics*. The Parabolic Press, Stanford, CA
84. Vo ND (1992) *Characteristics of curvilinear flow past circular-crested weirs*. Ph.D. Thesis. Concordia University, Canada

85. Webster WC, Shields JJ (1989) Conservation of mechanical energy and circulation in the theory of inviscid fluid sheets. *J Eng Math* 23(1):1–15
86. Webster WC, Shields JJ (1991) Applications of high-level, Green-Naghdi theory to fluid flow problems. Dynamics of marine vehicles and structures in waves. Elsevier, Amsterdam, pp 109–124
87. Webster WC, Kim DY (1990) The dispersion of large amplitude gravity waves in deep water. In: Proceedings of 18th symposium on naval hydrodynamics, Ann Arbor
88. Webster WC, Wehausen JV (1995) Bragg scattering of water waves by Green-Naghdi theory. *ZAMP* 46, special issue theoretical, experimental and numerical contributions to the mechanics of fluids and solids, S566–S583
89. Webster WC, Zhang X (1998) A waterfall springing from unsteady flow over an uneven bottom. In: International workshop on water waves and floating bodies 13 (IWWWFB13), 29 March–1 April 1998, Alphen aan den Rijn, Netherlands
90. Webster WC, Zhao B (2018) The development of a high-accuracy, broadband, Green-Naghdi model for steep, deep-water ocean waves. *J Ocean Eng Marine Energy* 4(1):273–291
91. Webster WC, Duan WY, Zhao BB (2011) Green-Naghdi theory, part A: green Naghdi (GN) equations for shallow water waves. *J Mar Sci Appl* 10:253–258
92. Williams ME, Stacey MT (2016) Tidally discontinuous ocean forcing in bar-built estuaries: the interaction of tides, infragravity motions, and frictional control. *J Geophys Res: Oceans* 121(1):571–585
93. Zhang Y, Kennedy AB, Panda N, Dawson C, Westerink JJ (2013) Boussinesq-Green-Naghdi rotational water wave theory. *Coast Eng* 73:13–27
94. Zhao BB, Duan WY (2010) Fully nonlinear shallow water waves simulation using Green–Naghdi theory. *J Mar Sci Appl* 9:1–7
95. Zhao BB, Duan WY, Ertekin RC (2014) Application of higher-level GN theory to some wave transformation problems. *Coast Eng* 83:177–189
96. Zhao BB, Ertekin RC, Duan WY, Hayatdavoodi M (2014) On the steady solitary-wave solution of the Green–Naghdi equations of different levels. *Wave Motion* 51(8):1382–1395
97. Zhao BB, Ertekin RC, Duan WY (2015) A comparative study of diffraction of shallow-water waves by high-level IGN and GN equations. *J Comput Phys* 283:129–147
98. Zhao BB, Duan WY, Ertekin RC, Hayatdavoodi M (2015) High-level Green–Naghdi wave models for non linear wave transformation in three dimensions. *J Ocean Eng Mar Energy* 1:121–132
99. Zheng K, Zhao BB, Duan WY, Ertekin RC, Chen XB (2016) Simulation of evolution of gravity wave groups with moderate steepness. *Ocean Model* 98:1–11

**Publisher's Note** Springer Nature remains neutral with regard to jurisdictional claims in published maps and institutional affiliations.

Springer Nature or its licensor (e.g. a society or other partner) holds exclusive rights to this article under a publishing agreement with the author(s) or other rightsholder(s); author self-archiving of the accepted manuscript version of this article is solely governed by the terms of such publishing agreement and applicable law.

## Authors and Affiliations

Oscar Castro-Orgaz<sup>1</sup> · Pedro P. Gamero-Ojeda<sup>1</sup> · Francisco N. Cantero-Chinchilla<sup>1</sup> · Tomás Morales de Luna<sup>2</sup> · Hubert Chanson<sup>3</sup>

✉ Oscar Castro-Orgaz  
ag2caoro@uco.es

Pedro P. Gamero-Ojeda  
ag2gaojp@uco.es

Francisco N. Cantero-Chinchilla  
z12cachf@uco.es

Tomás Morales de Luna  
tmorales@uma.es

Hubert Chanson  
h.chanson@uq.edu.au

- <sup>1</sup> Hydraulic Engineering Area, University of Cordoba, Rabanales Campus, Leonardo da Vinci Building, 14071 Córdoba, Spain
- <sup>2</sup> Dpto. de Anal. Matem., Estad. e I.O. y Matemática Aplicada, University of Málaga, Campus de Teatinos, 29071 Málaga, Spain
- <sup>3</sup> School of Civil Engineering, The University of Queensland, Brisbane, QLD 4072, Australia